

***u-p* Semi-Lagrangian Reproducing Kernel Formulation for Landslide Modeling**

Thanakorn Siriaksorn¹, Sheng-Wei Chi², Craig Foster³, and Ashkan Mahdavi⁴

¹Ph.D., Department of Civil and Materials Engineering, University of Illinois at Chicago, IL 60607, tsiria3@uic.edu

²Corresponding author, Assistant Professor, Department of Civil and Materials Engineering, University of Illinois at Chicago, IL 60607, swchi@uic.edu

³Associate Professor, Department of Civil and Materials Engineering, University of Illinois at Chicago, IL 60607

⁴Department of Civil and Materials Engineering, University of Illinois at Chicago, IL 60607

ABSTRACT

This paper presents a *u-p* (displacement-pressure) semi-Lagrangian Reproducing Kernel (RK) formulation to effectively analyze landslide processes. The semi-Lagrangian RK approximation is constructed based on Lagrangian discretization points with fixed kernel supports in the current configuration. As a result, it tracks state variables at discretization points while allowing extreme deformation and material separation that is beyond the capability of Lagrangian formulations. The *u-p* formulation following Biot theory is incorporated into the formulation to describe poromechanics of saturated geomaterials. In addition, a stabilized nodal integration method to ensure stability of the domain integration, and kernel contact algorithms to model contact between bodies, are introduced in the *u-p* semi-Lagrangian RK formulation. The proposed method is verified with several numerical examples and validated with an experimental result and the field data of an actual landslide.

1. INTRODUCTION

During the past century, much research has been done to mitigate the impact of landslides, which can cause considerable damage as well as loss of life [1-4]. While a well-controlled experiment can be effective to study and analyze landslide activities on a case-by-case basis, it requires considerable time, expense, and human labor. An alternative way is to perform a mathematical analysis of the slope. Early approaches to this problem include Limit Equilibrium Methods

(LEMs) [5] to analyze slope stability of a landscape. These techniques provide a relatively quick and tractable analysis of the stability of the slope. Nevertheless, LEMs neglect local deformation and consider only equilibrium conditions of an entire slope using a pre-defined slip surface [5], which limits their applicability to conduct more sophisticated slope stability analysis.

With the advancement of computational capabilities in the past two decades, numerical methods have been extensively employed and developed for landslide analysis. However, due to distinctive numerical challenges, numerical analysis of landslide processes is commonly separated into slope stability analysis and run-out simulation. To analyze slope stability, whose characteristics consist of complex poromechanics and solid-like behaviors, finite element methods (FEMs) with Lagrangian formulations are usually employed [1, 6, 7]. Although FEMs can accurately and effectively account for complex soil behaviors while the slope undergoes small deformation, they suffer significant difficulties due to severe mesh distortion and separation when slope experiences extreme deformation and propagates. As a result, run-out simulation, which involves extremely large deformation and material separation, are usually handled by methods such as smoothed particle hydrodynamics (SPH) [8-14] and the discrete element method (DEM) [15-17]. This is due to the discontinuum-based nature of SPH [18] and DEM [19], which is suitable with simulating flow-like phenomena. Nevertheless, SPH suffers from tensile instability and boundary deficiency since the kernel approximations are inconsistent [18], while parameters of element-to-element contact models used in DEM are difficult to calibrate and can significantly impair the accuracy [20]. Since it is extremely challenging or even impractical to apply one of these numerical methods to effectively and accurately analyze whole landslide processes, some researchers have suggested or employed coupled methods such as FEM-SPH [21] or FEM-DEM [22, 23], to handle different stages of landslide processes with suitable numerical methods by defining certain strain criteria to switch between methods. However, mathematical verification of the transition between two distinctive numerical methods is still not robust. Recently, Finite elements with Lagrangian Integration Points (FEM-LIP) have been applied to landslide problems [24, 25]. Developed from particle-in-cell methods, FEM-LIP has a fixed Eulerian background mesh with integration points that can flow through it. Constitutive models have been developed to model the transition from solid to fluid behavior, but the method still relies on a background mesh. These numerical issues demonstrate the necessity of a sophisticated yet effective numerical method that can both accurately analyze slope stability and simulate landslide run-out.

The Reproducing Kernel Particle Method (RKPM) [26, 27] has been proposed to eliminate the difficulties due to the strong mesh dependency of FEMs. The method introduces a correction function in the kernel approximations to satisfy the consistency conditions and partition of unity [28]. Hence, the RKPM can accurately analyze slope stability as FEM, while higher-order accuracy can be easily achieved by increasing the order of basis functions in the correction function. The method can also handle large deformation with ease [27, 29-31] since it requires only discrete points to construct approximation functions.

This paper presents an extension of the RKPM, the semi-Lagrangian RKPM, for analyzing entire landslide processes within one mathematical framework. Besides the capability to analyze slope stability as effectively as FEMs, the present method can also naturally model run-out simulation. This is due to the construction of the approximation functions in the current configuration [32, 33], which readily allows extreme deformation and material separation. Because of such principle, the method can also naturally detect contacting bodies with contact forces directly calculated from a constitutive model, which can be aided by a level-set algorithm [31] to enhance accuracy of the contacting surfaces. In addition, to preserve the mesh-free properties while maintaining stability, a stabilized nodal integration method called the Modified Stabilized Non-conforming Nodal Integration (MSNNI) [34] is incorporated in the framework. In this work, the domain integration method and contact algorithms are addressed in a two-field framework due to the incorporation of the two-field formulations using Biot theory [35] with the semi-Lagrangian RKPM to properly describe mechanics of porous media.

2. SATURATED DEFORMABLE POROUS MEDIA

In this study, the poromechanics of saturated deformable porous media is described using a saturated two-phase formulation extended from the Biot theory [36]. This is to take into account the coupling effect between solid and fluid phases, which is important to the mechanical behavior in most geomaterials. Only slow to moderate speed events, such as consolidation and landslide problems, are considered so the relative acceleration of the fluid with respect to the solid can be neglected [36].

Considering no phase change and isothermal conditions, the governing equations of the dynamic displacement-pressure (u - p) formulation can be described by

$$\text{Balance of momentum equation: } \sigma_{ij,j} + b_i = \rho \ddot{u}_i \quad \text{in } \Omega \quad (1)$$

$$\text{Continuity equation: } \alpha \dot{u}_{i,i} + \frac{\dot{P}^f}{M} + q_{i,i}^f = 0 \quad \text{in } \Omega \quad (2)$$

where σ_{ij} is the total stress, $b_i = \rho g_i$ is the body force, g_i is the acceleration of gravity, $\rho = (1-n)\rho^s + n\rho^f$ is the saturated density of porous medium, n is the porosity, ρ^s is the density of solid grains, ρ^f is the density of fluid f , u_i is the displacement of solid skeleton, and Ω is the problem domain. The Biot coefficient is defined as $\alpha \equiv 1 - K/K^s$, K is the bulk modulus of porous medium, K^s is the bulk modulus of solid grains, M is regarded as Biot compressibility modulus, and P^f and q_i^f are the pore fluid pressure and superficial velocity of fluid, respectively.

The Biot compressibility modulus M can be denoted by

$$\frac{1}{M} = \frac{\alpha - n}{K^s} + \frac{n}{K^f} \quad (3)$$

where K^f is the bulk modulus of fluid.

An isotropic Darcy's law is employed to describe fluid flow through an intrinsic permeability k ,

$$q_i^f = -\frac{k}{\mu^f} (P_{,i}^f - \rho^f g_i) \quad (4)$$

where μ^f is the dynamic viscosity of fluid.

Following Biot theory, the total stress σ_{ij} can be decomposed into the effective stress of solid phase $\bar{\sigma}_{ij}$ and the pore fluid pressure P^f by

$$\sigma_{ij} = \bar{\sigma}_{ij} - \alpha P^f \delta_{ij} \quad (5)$$

where δ_{ij} is the second-order identity tensor.

Since $\bar{\sigma}_{ij}$ is fully decoupled from the fluid phase, it can be computed using constitutive models of solid independent of the fluid phase. For demonstration purpose, the Drucker-Prager plasticity model with non-associated flow rule and a damage model adapted from [37] are used in this study to represent geomaterial behaviors.

The Drucker-Prager yield function is described as

$$f = \sqrt{2J_2} + BI_1 - k \quad (6)$$

where J_2 is the second invariant of the deviatoric part of $\hat{\sigma}_{ij}$; I_1 is the first invariant of $\hat{\sigma}_{ij}$; B and k are material parameters; $\hat{\sigma}_{ij}$ is the effective stress before attenuated by material damage. The Drucker-Prager material parameters B and k can be related to cohesion c and friction angle ϕ of Mohr-Coulomb by

$$B = \frac{2\sqrt{6} \sin \phi}{3(3 - \sin \phi)} \quad (7)$$

$$k = \frac{2\sqrt{6}c \cos \phi}{3 - \sin \phi} \quad (8)$$

For non-associated flow rule, the plastic potential function has different form from the yield function. In this paper, the plastic potential function takes the following form

$$g = \sqrt{2J_2} + \beta I_1 - k \quad (9)$$

where β can be related to dilatancy angle ψ as

$$\beta = \frac{2\sqrt{6} \sin \psi}{3(3 - \sin \psi)} \quad (10)$$

A damage parameter d is introduced to degrade the deviatoric part and the tensile volumetric part of the effective stress $\hat{\sigma}_{ij}$. It yields the total (damaged) effective stress $\bar{\sigma}_{ij}$ as

$$\bar{\sigma}_{ij} = \hat{\sigma}_{ij}^{\text{dev}} (1-d) + \left((1-d)\hat{\sigma}_{kk}^+ + \hat{\sigma}_{kk}^- \right) \delta_{ij} \quad (11)$$

where superscript dev, +, and - indicate deviatoric, tensile, and compressive parts of the corresponding terms, respectively. Following [32], the damage parameter d is defined as

$$d = \frac{c_1(\eta - c_2)}{\eta(c_1 - c_2)} \quad ; \quad \eta \geq c_2 \quad (12)$$

where η is the norm of the deviatoric strain (i.e., $\eta = \sqrt{\varepsilon_{ij}^{\text{dev}} \varepsilon_{ji}^{\text{dev}}}$) used as a means to identify material damage. The damage parameter c_2 specify the initiation point, when material starts to damage (i.e. $d = 0$). The damage parameter c_1 specify the critical point, when material is fully damaged (i.e. $d = 1$).

In addition, to take into account large deformation, the stress update is carried out following [38]

$$\bar{\sigma}_{ij}^{n+1} = T_{ik}^{n+1} \bar{\sigma}_{kl}^n T_{lj}^{n+1} + C_{ijkl}^{\text{dmg}} \Delta \varepsilon_{kl}^{n+0.5} \quad (13)$$

where C_{ijkl}^{dmg} is elasto-plastic-damage material tangent tensor. T_{ik}^{n+1} and T_{lj}^{n+1} are the transformation matrices denoted by

$$T_{ij}^{n+1} = \delta_{ij} + \left(\delta_{ik} - \frac{1}{2} w_{ik}^{n+0.5} \right)^{-1} w_{kj}^{n+0.5} \quad (14)$$

$$\text{with} \quad w_{ij}^{n+0.5} = \Delta u_{[i,j]}^{n+0.5} = \frac{1}{2} \left(\frac{\partial \Delta u_i}{\partial x_j^{n+0.5}} - \frac{\partial \Delta u_j}{\partial x_i^{n+0.5}} \right) \quad (15)$$

The incremental strain $\Delta \varepsilon_{kl}^{n+0.5}$ can be expressed as

$$\Delta \varepsilon_{kl}^{n+0.5} = \Delta u_{(i,j)}^{n+0.5} = \frac{1}{2} \left(\frac{\partial \Delta u_i}{\partial x_j^{n+0.5}} + \frac{\partial \Delta u_j}{\partial x_i^{n+0.5}} \right) \quad (16)$$

$$\text{with} \quad \frac{\partial \Delta u_i}{\partial x_j^{n+0.5}} = \frac{\partial \Delta u_i}{\partial x_j} \frac{\partial x_j}{\partial x_j^{n+0.5}} \quad (17)$$

The superscript $n+0.5$ denotes that the corresponding variables are evaluated from the configuration at time step $n+0.5$, which minimizes the error [38].

The corresponding boundary and initial conditions of the governing equations (1) and (2) are defined as

$$\begin{aligned}
\sigma_{ij} n_j &= h_i & \text{on } \Gamma_h \\
u_i &= u_i^g & \text{on } \Gamma_g \\
-q_i^f n_i^f &= v_s^f & \text{on } \Gamma_s \\
P^f &= P_r^f & \text{on } \Gamma_r \\
u_i(\mathbf{x}, t=0) &= u_i^0(\mathbf{x}) & \text{in } \Omega \\
\dot{u}_i(\mathbf{x}, t=0) &= \dot{u}_i^0(\mathbf{x}) & \text{in } \Omega \\
P^f(\mathbf{x}, t=0) &= P_0^f(\mathbf{x}) & \text{in } \Omega
\end{aligned} \tag{18}$$

where n_j and n_i^f are the unit normal vectors in the outward direction of corresponding boundaries Γ_h and Γ_s . In Eq. (18), h_i is the prescribed traction on Γ_h ; u_i^g is the prescribed displacement on Γ_g ; v_s^f is the prescribed fluid inflow on Γ_s ; P_r^f is the prescribed pore fluid pressure on Γ_r ; Γ is the boundary of Ω and has the following relationships: $\Gamma_h \cup \Gamma_g = \Gamma$, $\Gamma_h \cap \Gamma_g = \emptyset$, $\Gamma_s \cup \Gamma_r = \Gamma$, and $\Gamma_s \cap \Gamma_r = \emptyset$; the initial values of displacement and velocity of the porous medium are denoted by $u_i^0(\mathbf{x})$ and $\dot{u}_i^0(\mathbf{x})$, respectively; $P_0^f(\mathbf{x})$ is the initial value of the pore fluid pressure. Only water is considered in this work, as the fluid phase, and hence the superscript f will be replaced by w hereafter. Additionally, the superscript w on the pore water pressure P^w will be dropped for simplicity.

Applying the boundary conditions (18) into the governing equations (1) and (2), the variational equations of the u - p formulation are obtained as

$$\int_{\Omega} \delta u_{i,j} \bar{\sigma}_{ij} d\Omega - \int_{\Omega} \delta u_{i,i} \alpha P d\Omega + \int_{\Omega} \delta u_i \rho \ddot{u}_i d\Omega = \int_{\Gamma_h} \delta u_i h_i d\Gamma + \int_{\Omega} \delta u_i b_i d\Omega \tag{19}$$

$$\int_{\Omega} \delta P \alpha \dot{u}_{i,i} d\Omega + \int_{\Omega} \delta P \frac{\dot{P}}{M} d\Omega + \int_{\Omega} \delta P_{,i} \frac{k}{\mu^w} P_{,i} d\Omega = \int_{\Gamma_s} \delta P v_s^w d\Gamma + \int_{\Omega} \delta P_{,i} \frac{k}{\mu^w} \rho^w g_i d\Omega \tag{20}$$

with the corresponding Galerkin approximation as follows

$$\int_{\Omega} \delta u_{i,j}^h \bar{\sigma}_{ij}^h d\Omega - \int_{\Omega} \delta u_{i,i}^h \alpha P^h d\Omega + \int_{\Omega} \delta u_i^h \rho \ddot{u}_i^h d\Omega = \int_{\Gamma_h} \delta u_i^h h_i d\Gamma + \int_{\Omega} \delta u_i^h b_i d\Omega \tag{21}$$

$$\int_{\Omega} \delta P^h \alpha \dot{u}_{i,i}^h d\Omega + \int_{\Omega} \delta P^h \frac{\dot{P}^h}{M} d\Omega + \int_{\Omega} \delta P_{,i}^h \frac{k}{\mu^w} P_{,i}^h d\Omega = \int_{\Gamma_s} \delta P^h v_s^w d\Gamma + \int_{\Omega} \delta P_{,i}^h \frac{k}{\mu^w} \rho^w g_i d\Omega \tag{22}$$

where superscript h denotes approximated function of the corresponding term.

3. SEMI-LAGRANGIAN RKPM

In the Lagrangian formulation, mapping between current configuration and initial configuration is required, i.e., $\mathbf{x} = \varphi(\mathbf{X}, t)$. Here \mathbf{X} refers to the Lagrangian coordinates, \mathbf{x} refers to the Eulerian coordinates, and φ is the mapping function. This mapping between the two configurations breaks down when extreme deformation occurs. To circumvent such issue, the shape functions of semi-Lagrangian RKPM [31, 32] are constructed in the current configuration, thus avoiding the severe distortion or even separation of the support domain. The discretization (i.e., nodal points) of semi-Lagrangian RK formulation, however, still follow a Lagrangian description to track internal variables of the same material points at each time step while the support of the RK shape function maintains a fixed shape and size. These properties of semi-Lagrangian RKPM, illustrated in Figure 1, are advantageous for problems involving extremely large deformation and material separation.

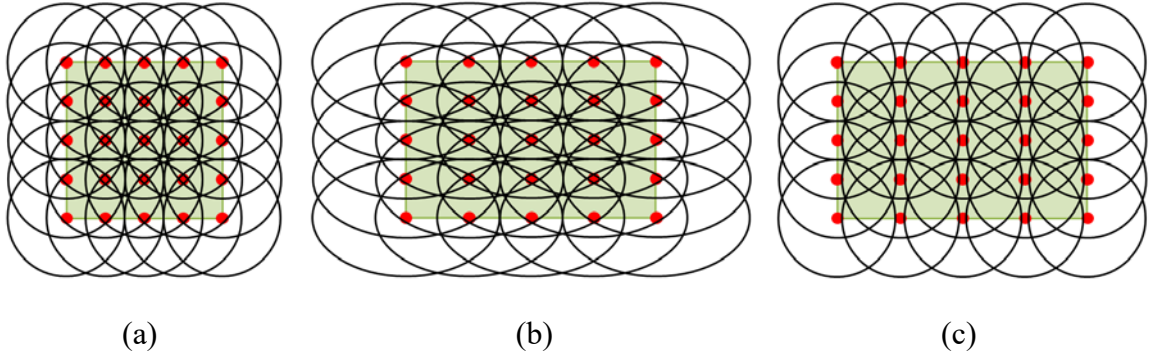


FIG. 1. Comparison between 2-D (a) RK shape functions in the initial configuration, (b) Lagrangian RK shape functions in the current configuration, and (c) semi-Lagrangian RK shape functions in the current configuration.

The semi-Lagrangian RK shape functions are defined as

$$\Psi_I(\mathbf{x}) = C(\mathbf{x}; \mathbf{x} - \mathbf{x}_I) \Phi_a(\mathbf{x} - \mathbf{x}_I) \quad (23)$$

where $\Psi_I(\mathbf{x})$ is the shape function of node I constructed in the current configuration and $\mathbf{x}_I = \mathbf{x}(\mathbf{X}_I, t)$ is the nodal position of node I in the current configuration. The correction function $C(\mathbf{x}; \mathbf{x} - \mathbf{x}_I)$ and the kernel function $\Phi_a(\mathbf{x} - \mathbf{x}_I)$ are also determined in the current configuration. The kernel function controls the smoothness and locality of the approximation function, and hence it should be selected depending on the characteristics of the problem, e.g., the order of partial differential equations. For m -dimensional analysis, the m -dimensional kernel function can be constructed by the product of one dimensional kernel function; that is

$$\Phi_a^{m-D}(\mathbf{x} - \mathbf{x}_I) = \prod_{i=1}^m \Phi_a^{1-D}(z_i) \quad (24)$$

$$\text{with} \quad z_i = \frac{|x_i - x_{iI}|}{a_i} \quad (25)$$

where a is a number defining the influence domain, also called the support size of the function. This value is usually normalized by nodal distance and called the normalized support size $\tilde{a} = a/\Delta x$.

The correction function is introduced to enforce the reproducing conditions to achieve reproducibility for monomials up to the specified n^{th} order consistency, that is

$$C(\mathbf{x}; \mathbf{x} - \mathbf{x}_I) = \sum_{|\alpha|=0}^n (\mathbf{x} - \mathbf{x}_I)^\alpha b_\alpha(\mathbf{x}) \quad (26)$$

where $\alpha = (\alpha_1, \alpha_2, \dots, \alpha_m)$ with its length defined as $|\alpha| \equiv \sum_{i=1}^m \alpha_i$ and $b_\alpha \equiv b_{\alpha_1, \alpha_2, \dots, \alpha_m}$ is the corresponding coefficient of the monomials $(\mathbf{x} - \mathbf{x}_I)^\alpha \equiv (x_1 - x_{1I})^{\alpha_1} (x_2 - x_{2I})^{\alpha_2} \dots (x_m - x_{mI})^{\alpha_m}$.

The coefficients $\mathbf{b}(\mathbf{x})$ are obtained by satisfying the n^{th} order reproducing condition

$$\sum_{I=1}^{NP} \Psi_I(\mathbf{x}) \mathbf{x}_I^\alpha = \mathbf{x}^\alpha \quad ; \quad |\alpha| \leq n \quad (27)$$

where NP is the total number of nodes. By using Eqs. (23) and (26) and imposing the reproducing condition (27), the corresponding coefficients $\mathbf{b}(\mathbf{x})$ can be determined as

$$\mathbf{b}(\mathbf{x}) = \mathbf{M}^{-1}(\mathbf{x}) \mathbf{H}(\mathbf{0}) \quad (28)$$

where $\mathbf{M}(\mathbf{x})$ is the moment matrix which can be described in discrete form as

$$\mathbf{M}(\mathbf{x}) = \sum_{I=1}^{NP} \mathbf{H}(\mathbf{x} - \mathbf{x}_I) \mathbf{H}^T(\mathbf{x} - \mathbf{x}_I) \Phi_a(\mathbf{x} - \mathbf{x}_I) \quad (29)$$

and $\mathbf{H}(\mathbf{x} - \mathbf{x}_I)$ is the vector of monomial basis functions.

Substituting Eq. (28) into Eqs. (26) and (23), the semi-Lagrangian RK shape function reads

$$\Psi_I(\mathbf{x}) = \mathbf{H}^T(\mathbf{0}) \mathbf{M}^{-1}(\mathbf{x}) \mathbf{H}(\mathbf{x} - \mathbf{x}_I) \Phi_a(\mathbf{x} - \mathbf{x}_I) \quad (30)$$

Therefore, a function Y_i can be approximated by using semi-Lagrangian RK approximation

$\Psi_I(\mathbf{x})$ constructed based on a set of distinct points $\{\mathbf{x}_I\}_{I=1}^{NP}$ and its corresponding nodal coefficient $y_{iI}(t)$, that is

$$Y_i^h(\mathbf{x}, t) = \sum_{I=1}^{NP} \Psi_I(\mathbf{x}) y_{il}(t) \quad (31)$$

Subsequently, the approximation of the temporal derivative of function Y_i is expressed as

$$\dot{Y}_i^h(\mathbf{x}, t) = \sum_{I=1}^{NP} (\Psi_I(\mathbf{x}) \dot{y}_{il}(t) + \bar{\Psi}_I(\mathbf{x}) y_{il}(t)) \quad (32)$$

where $\dot{y}_{il}(t)$ is the nodal coefficient corresponding to $\dot{Y}_i^h(\mathbf{x}, t)$. $\bar{\Psi}_I(\mathbf{x})$ is the change of the RK shape function with respect to time, due to the reconstruction of the semi-Lagrangian RK shape function, which can be interpreted as a convection term to carry the information history during the transition between the old shape function and the new one. It is defined as

$$\bar{\Psi}_I(\mathbf{x}) = C(\mathbf{x}; \mathbf{x} - \mathbf{x}_I) \dot{\Phi}_a(\mathbf{x} - \mathbf{x}_I) \quad (33)$$

where the temporal derivative of the correction function is omitted since the function is constructed by solving the corresponding coefficient $\mathbf{b}(\mathbf{x})$ under the current configuration. The temporal derivative of the kernel function $\dot{\Phi}_a(\mathbf{x} - \mathbf{x}_I)$ is constructed by using Eq. (24) and performing the chain rule

$$\dot{\Phi}_a(\mathbf{x} - \mathbf{x}_I) = \prod_{i=1}^m \left(\frac{1}{a_i} \cdot \frac{\partial \Phi_a^{m-D}(z_i)}{\partial(z_i)} \cdot \frac{x_i - x_{il}}{|x_i - x_{il}|} \cdot \frac{\partial(x_i - x_{il})}{\partial t} \right). \quad (34)$$

4. SEMI-LAGRANGIAN RK FORMULATION FOR SATURATED DEFORMABLE POROUS MEDIA

Two cases of u - p formulation are considered in this paper: dynamic analysis and quasi-static analysis. For dynamic case, the formulations are as shown in Eqs. (1) and (2). However, for quasi-static case, the inertial term in Eq. (1) is omitted, which is only suitable with slow motion events [36]. Both cases are spatially discretized by the semi-Lagrangian RK while the temporal domain is discretized by different schemes for each case. The implicit temporal integration scheme is employed in the quasi-static case, whereas explicit time discretization is used for dynamic analysis due to higher efficiency. Explicit dynamics have been shown to be well suited for larger scale and faster motion problems such as landslides.

4.1 Spatial Discretization

The approximated displacement u_i^h , pore water pressure P^h , and their spatial derivatives with respect to current configuration in Eqs. (21) and (22) are expressed by the semi-Lagrangian RK approximation (31) as

$$u_i^h(\mathbf{x}, t) = \sum_{I=1}^{NP} \Psi_I(\mathbf{x}) d_{il}(t) \quad , \quad u_{i,j}^h(\mathbf{x}, t) = \sum_{I=1}^{NP} \Psi_{I,j}(\mathbf{x}) d_{il}(t) \quad (35)$$

$$P^h(\mathbf{x}, t) = \sum_{I=1}^{NP} \Psi_I(\mathbf{x}) p_I(t) \quad , \quad P_i^h(\mathbf{x}, t) = \sum_{I=1}^{NP} \Psi_{I,i}(\mathbf{x}) p_I(t) \quad (36)$$

where $d_{il}(t)$ and $p_I(t)$ are nodal coefficients of displacement and pore water pressure, respectively. For efficiency propose, the same linear-order semi-Lagrangian RK shape functions are adopted for both the displacement and the pore pressure fields in this study.

Remark:

It is well known that the approximations for the displacement and the pressure should be properly selected, according to the inf-sup or Ladyzhenskaya-Babuška-Brezzi (LBB) condition [39-41] to avoid pressure oscillations, which ultimately leads to numerical instability. Although adopting the same linear semi-Lagrangian RK shape functions for the displacement and pressure fields violates the LBB condition, the domain integration methods, namely nodal integration, described in the succeeding section alleviate the LBB instability issue. The nodal integration schemes under-integrate the strain energy, causing a similar effect as the reduced integration techniques in FEM [36]. As shown in Section 5, no instability condition has been observed in the problem where the equal order u-p FEM typically fails to provide a stable solution. It is, however, reported in [42] that the instability still occurs for problems with low permeability or under undrained conditions when a nodal integration scheme is employed. In such a case, a pressure projection scheme can be introduced to project the linear pressure field onto a piecewise-constant field. The difference between the linear pressure field and the projected constant field can be added into the continuity equation (22) as a stabilization to overcome the deficiency of equal-order approximation. For details, the reader is referred to [42-44].

The temporal derivatives of approximated displacement u_i^h and pore water pressure P^h in Eqs. (21) and (22) are expressed by the semi-Lagrangian RK approximation (31) as

$$\dot{u}_i^h(\mathbf{x}, t) = v_i^h(\mathbf{x}, t) = \sum_{I=1}^{NP} \left(\Psi_I(\mathbf{x}) v_{il}(t) + \bar{\Psi}_I(\mathbf{x}) d_{il}(t) \right) \quad (37)$$

$$\ddot{u}_i^h(\mathbf{x}, t) = a_i^h(\mathbf{x}, t) = \sum_{I=1}^{NP} \left(\Psi_I(\mathbf{x}) a_{il}(t) + 2\bar{\Psi}_I(\mathbf{x}) v_{il}(t) + \bar{\bar{\Psi}}_I(\mathbf{x}) d_{il}(t) \right) \quad (38)$$

$$\dot{P}^h(\mathbf{x}, t) = \sum_{I=1}^{NP} \left(\Psi_I(\mathbf{x}) \dot{p}_I(t) + \bar{\Psi}_I(\mathbf{x}) p_I(t) \right) \quad (39)$$

where v_i denotes the velocity, $v_{il}(t)$ is the nodal coefficient of velocity, a_i is the acceleration, $a_{il}(t)$ is the nodal coefficient of acceleration, and $\bar{\bar{\Psi}}_I(\mathbf{x})$ is the change of $\bar{\Psi}_I(\mathbf{x})$ with respect to time.

The semi-discrete form of Eqs. (21) and (22) are obtained by applying Eqs. (35) - (39) as

$$\begin{aligned} & \delta d_{li} \int_{\Omega} \Psi_{I,j} \bar{\sigma}_{ij}^h d\Omega - \delta d_{li} \int_{\Omega} \Psi_{I,i} \alpha \Psi_J d\Omega p_J + \delta d_{li} \int_{\Omega} \Psi_I \rho \Psi_J d\Omega a_{ij} \\ & + \delta d_{li} \int_{\Omega} 2 \Psi_I \rho \bar{\Psi}_J d\Omega v_{ij} + \delta d_{li} \int_{\Omega} \Psi_I \rho \bar{\bar{\Psi}}_J d\Omega d_{ij} = \delta d_{li} \int_{\Gamma_h} \Psi_I h_i d\Gamma + \delta d_{li} \int_{\Omega} \Psi_I b_i d\Omega \end{aligned} \quad (40)$$

$$\begin{aligned} & \delta p_I \int_{\Omega} \Psi_I \alpha \Psi_{J,i} d\Omega v_{ij} + \delta p_I \int_{\Omega} \Psi_I \alpha \bar{\Psi}_{J,i} d\Omega d_{ij} + \delta p_I \int_{\Omega} \frac{\Psi_I \Psi_J}{M} d\Omega \dot{p}_J + \delta p_I \int_{\Omega} \frac{\Psi_I \bar{\Psi}_J}{M} d\Omega p_J \\ & + \delta p_I \int_{\Omega} \Psi_{I,i} \frac{k}{\mu^w} \Psi_{J,i} d\Omega p_J = \delta p_I \int_{\Gamma_s} \Psi_I v_s^w d\Gamma + \delta p_I \int_{\Omega} \Psi_{I,i} \frac{k}{\mu^w} \rho^w g_i d\Omega \end{aligned} \quad (41)$$

where the summation convention of repeating indices is employed. Dirichlet boundary conditions in the study are directly imposed by using RK shape functions with nodal interpolation property [45].

4.2 Temporal integration

Consider the semi-discrete dynamic u - p equations in Eqs. (40) and (41). The central difference and the forward Euler temporal integration schemes are employed for the displacement field and the pressure field, respectively, as follows.

$$d_{il}^{n+1} = d_{il}^n + \Delta t v_{il}^n + 0.5 \Delta t^2 a_{il}^n \quad (42)$$

$$v_{il}^{n+1} = \hat{v}_{il}^{n+1} + 0.5 \Delta t a_{il}^{n+1} \quad (43)$$

$$p_I^{n+1} = p_I^n + \Delta t \dot{p}_I^n \quad (44)$$

where Δt is the time step. The predicted velocity \hat{v}_{il}^{n+1} is defined as

$$\hat{v}_{il}^{n+1} = v_{il}^n + 0.5 \Delta t a_{il}^n \quad (45)$$

The semi-discrete equations (40) and (41) are recast into matrix forms:

$$\mathbf{M} \mathbf{a}^{n+1} + \mathbf{G} \mathbf{v}^{n+1} + \bar{\mathbf{G}} \mathbf{d}^{n+1} = \mathbf{F}^{\text{ext}} - \mathbf{F}^{\text{int}} \quad (46)$$

$$\mathbf{S} \mathbf{p}^{n+1} + \tilde{\mathbf{G}} \mathbf{p}^{n+1} + \tilde{\tilde{\mathbf{G}}} \mathbf{d}^{n+1} = \tilde{\mathbf{F}}^{\text{ext}} - \tilde{\mathbf{F}}^{\text{int}} \quad (47)$$

where

$$M_{il} = \int_{\Omega} \Psi_I \rho \Psi_J d\Omega \quad (48)$$

$$S_{IJ} = \int_{\Omega} \frac{\Psi_I \Psi_J}{M} d\Omega \quad (49)$$

$$G_{IJ} = \int_{\Omega} 2\Psi_I \rho \bar{\Psi}_J d\Omega \quad (50)$$

$$\bar{G}_{IJ} = \int_{\Omega} \Psi_I \rho \bar{\bar{\Psi}}_J d\Omega \quad (51)$$

$$\tilde{G}_{IJ} = \int_{\Omega} \frac{\Psi_I \bar{\Psi}_J}{M} d\Omega \quad (52)$$

$$\tilde{\tilde{G}}_{IJ} = \int_{\Omega} \Psi_I \alpha \bar{\Psi}_{J,i} d\Omega \quad (53)$$

$$F_{il}^{\text{ext}} = \int_{\Gamma_h} \Psi_I h_i d\Gamma \quad (54)$$

$$\tilde{F}_I^{\text{ext}} = \int_{\Gamma_s} \Psi_I v_s^w d\Gamma \quad (55)$$

$$F_{il}^{\text{int}} = \int_{\Omega} \Psi_{I,j} \bar{\sigma}_{ij}^h d\Omega - \int_{\Omega} \Psi_{I,i} \alpha \Psi_J d\Omega p_J^{n+1} - \int_{\Omega} \Psi_I b_i d\Omega \quad (56)$$

$$\tilde{F}_I^{\text{int}} = \int_{\Omega} \Psi_I \alpha \Psi_{J,i} d\Omega v_{IJ}^{n+1} + \int_{\Omega} \Psi_{I,i} \frac{k}{\mu^w} \Psi_{J,i} d\Omega p_J^{n+1} - \int_{\Omega} \Psi_{I,i} \frac{k}{\mu^w} \rho^w g_i d\Omega. \quad (57)$$

Introducing a mass proportional damping \mathbf{C} and applying the temporal integration schemes in (42) - (45) to (46) and (47), the fully discrete equations read

$$(\mathbf{M} + 0.5\Delta t(\mathbf{C} + \mathbf{G})) \mathbf{a}^{n+1} = \mathbf{F}^{\text{ext}} - \mathbf{F}^{\text{int}} - (\mathbf{C} + \mathbf{G}) \hat{\mathbf{v}}^{n+1} - \bar{\mathbf{G}} \mathbf{d}^{n+1} \quad (58)$$

$$\mathbf{S} \dot{\mathbf{p}}^{n+1} = \tilde{\mathbf{F}}^{\text{ext}} - \tilde{\mathbf{F}}^{\text{int}} - \tilde{\tilde{\mathbf{G}}} \mathbf{d}^{n+1} - \tilde{\mathbf{G}} \mathbf{p}^{n+1} \quad (59)$$

The matrices associated with the time rate change of the semi-Lagrangian kernels, \mathbf{G} , $\bar{\mathbf{G}}$, $\tilde{\tilde{\mathbf{G}}}$, and $\tilde{\mathbf{G}}$, can be omitted for computational efficiency since they have very subtle effects on the solutions when the relative nodal velocity in (38) are small to moderate (see [31, 33]), which is generally true in the problems studied in the paper. A one-dimensional wave propagation problem is given in Appendix B to demonstrate that the effect of \mathbf{G} and $\bar{\mathbf{G}}$ on the solution is negligible.

Equations (58) and (59), therefore, degenerate to

$$(\mathbf{M} + 0.5\Delta t \mathbf{C}) \mathbf{a}^{n+1} = \mathbf{F}^{\text{ext}} - \mathbf{F}^{\text{int}} - \mathbf{C} \hat{\mathbf{v}}^{n+1} \quad (60)$$

$$\mathbf{S} \dot{\mathbf{p}}^{n+1} = \tilde{\mathbf{F}}^{\text{ext}} - \tilde{\mathbf{F}}^{\text{int}} \quad (61)$$

In this paper, 5% mass proportional damping is used for \mathbf{C} and the lumped mass scheme by conducting the row sum is employed for \mathbf{M} and \mathbf{S} to acquire diagonal matrices. This process can uncouple the system of equations and significantly improve computational efficiency

without significantly impairing accuracy, which will be shown in the first numerical example. At each time step, a_{il}^{n+1} is solved from Eq. (60), then v_{il}^{n+1} is updated by Eq. (43), and \dot{p}_l^{n+1} is subsequently determined by using Eq. (61).

Even though the efficiency of the explicit temporal integration schemes are attractive, implicit temporal integration schemes offer better stability, which may be required in problems where the critical time step size is prohibitively small or unconditionally unstable result occurs in the explicit scheme, as shown in [46]. However, due to the computational cost of the implicit temporal integration, this approach will only be used for benchmark (small scale) problems in this paper for verification purpose.

When slow-motion phenomena are considered, the inertia forces in the equation of motion can be neglected, leading to the u - p quasi-static formulation. The semi-discrete form of Eqs. (21) and (22) can be rewritten in matrix forms as

$$\mathbf{Kd}^{n+1} - \mathbf{Qp}^{n+1} = \mathbf{F}^* \quad (62)$$

$$\mathbf{Q}^T \mathbf{v}^{n+1} + \tilde{\mathbf{G}} \mathbf{d}^{n+1} + \mathbf{Sp}^{n+1} + \tilde{\mathbf{G}} \mathbf{p}^{n+1} + \mathbf{Hp}^{n+1} = \tilde{\mathbf{F}}^* \quad (63)$$

where

$$\left. \begin{aligned} K_{ikll} &= \int_{\Omega} \Psi_{l,j} C_{ijkl}^{\text{dmg}} \Psi_{j,l} d\Omega, \quad Q_{ill} = \int_{\Omega} \Psi_{l,i} \alpha \Psi_j d\Omega, \\ F_{il}^* &= \int_{\Gamma_h} \Psi_l h_i d\Gamma + \int_{\Omega} \Psi_l b_i d\Omega, \quad H_{ll} = \int_{\Omega} \Psi_{l,i} \frac{k}{\mu^w} \Psi_{j,i} d\Omega, \\ \tilde{F}_l^* &= \int_{\Gamma_s} \Psi_l v_s^w d\Gamma + \int_{\Omega} \Psi_{l,i} \frac{k}{\mu^w} \rho^w g_i d\Omega \end{aligned} \right\} \quad (64)$$

As described in dynamic case, convection terms can be negligible resulted in

$$\mathbf{Kd}^{n+1} - \mathbf{Qp}^{n+1} = \mathbf{F}^* \quad (65)$$

$$\mathbf{Q}^T \mathbf{v}^{n+1} + \mathbf{Sp}^{n+1} + \mathbf{Hp}^{n+1} = \tilde{\mathbf{F}}^* \quad (66)$$

Only the first order temporal derivative of displacement and pore water pressure is involved in Eqs. (62) and (63); therefore, backward Euler method is employed for the temporal integration of both displacement and pore water pressure. At time step $n+1$, the displacement and pore water pressure can be expressed as

$$d_{il}^{n+1} = d_{il}^n + \Delta t v_{il}^{n+1} = d_{il}^n + \Delta d_{il}^{n+1} \quad (67)$$

$$p_l^{n+1} = p_l^n + \Delta t \dot{p}_l^{n+1} = p_l^n + \Delta p_l^{n+1} \quad (68)$$

Applying temporal integration (Eqs. (67) and (68)) in Eqs. (65) and (66), then rearranging the equations to recover the symmetry as follows

$$\begin{bmatrix} \mathbf{K} & -\mathbf{Q} \\ -\mathbf{Q}^T & -\mathbf{S} - \Delta t \mathbf{H} \end{bmatrix} \begin{Bmatrix} \Delta \mathbf{d}^{n+1} \\ \Delta \mathbf{p}^{n+1} \end{Bmatrix} = \begin{Bmatrix} \mathbf{F}^* - \mathbf{K} \mathbf{d}^n + \mathbf{Q} \mathbf{p}^n \\ -\Delta t \tilde{\mathbf{F}}^* + \Delta t \mathbf{H} \mathbf{p}^n \end{Bmatrix} \quad (69)$$

At each time step, the incremental displacement Δd_{il}^{n+1} and incremental pore water pressure Δp_l^{n+1} are solved simultaneously from Eq. (69), then d_{il}^{n+1} and p_l^{n+1} are updated by Eqs. (67) and (68), respectively.

4.3 u - p Stabilized Nodal Integration Method

One of the most important issues in the Galerkin formulation using semi-Lagrangian RK approximation is the domain integration. This is primarily due to the nature of RK approximation and the applications of semi-Lagrangian RKPM, which usually involves extreme deformation and discontinuities [47]. Nodal integration methods are especially effective for problems with such characteristics. However, direct nodal integration method suffers from rank deficiency due to under sampling and the derivative of a RK shape function vanishing at the node [48, 49]. To remedy the instability caused by rank deficiency and also achieve computational efficiency for large deformation problems, the Stabilized Non-conforming Nodal Integration (SNNI) [33] uses the idea of the assumed strain $\bar{\varepsilon}_{ij}^h$ from the Stabilized Conforming Nodal Integration (SCNI) [50] to construct the smoothed derivative of shape function over the pre-defined nodal representative domain (Figure 2b), that is

$$\bar{\varepsilon}^h(\mathbf{x}_L) = \sum_{I=1}^{NP} \bar{\mathbf{B}}_I(\mathbf{x}_L) \mathbf{d}_I \quad (70)$$

$$\text{with} \quad \bar{\mathbf{B}}_I^T(\mathbf{x}_L) = \begin{bmatrix} \bar{b}_{I1}(\mathbf{x}_L) & 0 & 0 & 0 & \bar{b}_{I3}(\mathbf{x}_L) & \bar{b}_{I2}(\mathbf{x}_L) \\ 0 & \bar{b}_{I2}(\mathbf{x}_L) & 0 & \bar{b}_{I3}(\mathbf{x}_L) & 0 & \bar{b}_{I1}(\mathbf{x}_L) \\ 0 & 0 & \bar{b}_{I3}(\mathbf{x}_L) & \bar{b}_{I2}(\mathbf{x}_L) & \bar{b}_{I1}(\mathbf{x}_L) & 0 \end{bmatrix} \quad (71)$$

$$\text{and} \quad \bar{b}_{ii}(\mathbf{x}_L) = \frac{1}{V_L} \int_{\Gamma_L} \Psi_I(\mathbf{x}) n_i(\mathbf{x}) d\Gamma \quad (72)$$

where V_L and Γ_L are the volume and boundary, respectively, of the nodal representative domain L . \mathbf{d}_I is the vector of corresponding nodal coefficient of displacement or so-called generalized displacement.

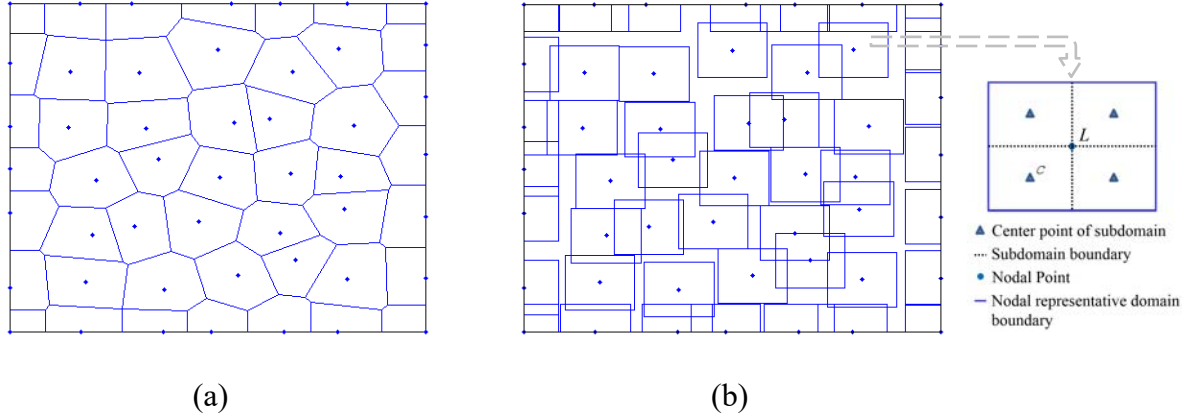


FIG. 2. Nodal representative domains of (a) SCNI and (b) SNNI in 2-D.

To be effective with the common applications of the semi-Lagrangian RKPM, the conforming restriction of each nodal representative domain, which aids SCNI in satisfying the integration constraints [50], is relaxed in SNNI by using a pre-defined nodal representative domain (Figure 2). In this work, the smoothed gradient of shape function is also used for pore water pressure as

$$\bar{\nabla} \mathbf{P}^h(\mathbf{x}_L) = \sum_{I=1}^{NP} \bar{\mathbf{B}}_I^p(\mathbf{x}_L) p_I \quad (73)$$

with

$$\bar{\mathbf{B}}_I^p(\mathbf{x}_L) = \begin{bmatrix} \bar{b}_{I1}(\mathbf{x}_L) \\ \bar{b}_{I2}(\mathbf{x}_L) \\ \bar{b}_{I3}(\mathbf{x}_L) \end{bmatrix} \quad (74)$$

where $\bar{\nabla} \mathbf{P}^h(\mathbf{x}_L)$ is the smoothed gradient of pore water pressure at node L .

For the explicit temporal integration, Eqs. (60) and (61) are numerically integrated by SNNI as

$$\left. \begin{aligned} \mathbf{F}_I^{\text{ext}} &= \sum_{K=1}^{NP} \Psi_I(\mathbf{x}_K) \mathbf{h}(\mathbf{x}_K) A_K, \quad \tilde{F}_I^{\text{ext}} = \sum_{K=1}^{NP} \Psi_I(\mathbf{x}_K) v_s^w(\mathbf{x}_K) A_K, \\ \mathbf{F}_I^{\text{int}} &= \sum_{L=1}^{NP} \bar{\mathbf{B}}_I^T(\mathbf{x}_L) \bar{\boldsymbol{\sigma}}(\mathbf{x}_L) V_L - \sum_{L=1}^{NP} \bar{\mathbf{B}}_I^T(\mathbf{x}_L) \alpha \Psi_J(\mathbf{x}_L) V_L p_J^{n+1} - \sum_{L=1}^{NP} \Psi_I(\mathbf{x}_L) \mathbf{b}(\mathbf{x}_L) V_L, \\ \tilde{F}_I^{\text{int}} &= \sum_{L=1}^{NP} \Psi_I(\mathbf{x}_L) \alpha \bar{\mathbf{B}}_J(\mathbf{x}_L) V_L v_J^{n+1} + \sum_{L=1}^{NP} \bar{\mathbf{B}}_I^{p,T}(\mathbf{x}_L) \frac{k}{\mu^w} \bar{\mathbf{B}}_J^p(\mathbf{x}_L) V_L p_J^{n+1} - \sum_{L=1}^{NP} \bar{\mathbf{B}}_I^{p,T}(\mathbf{x}_L) \frac{k}{\mu^w} \rho^w \mathbf{g} V_L \end{aligned} \right\} \quad (75)$$

where A_K is the boundary integration weight associated with node K and V_L is the nodal volume associated with node L .

For the implicit temporal integration, Eq. (69) is numerically integrated by SNNI as

$$\left. \begin{aligned} \mathbf{K}_{IJ} &= \sum_{L=1}^{NP} \bar{\mathbf{B}}_I^T(\mathbf{x}_L) \mathbf{C}^{\text{dmg}} \bar{\mathbf{B}}_J(\mathbf{x}_L) V_L, \quad \mathbf{Q}_{IJ} = \sum_{L=1}^{NP} \bar{\mathbf{B}}_I^T(\mathbf{x}_L) \alpha \Psi_J(\mathbf{x}_L) V_L, \\ H_{IJ} &= \sum_{L=1}^{NP} \bar{\mathbf{B}}_I^{p,T}(\mathbf{x}_L) \frac{k}{\mu^w} \bar{\mathbf{B}}_J^p(\mathbf{x}_L) V_L, \quad S_{IJ} = \sum_{L=1}^{NP} \frac{\Psi_I(\mathbf{x}_L) \Psi_J(\mathbf{x}_L)}{M} V_L, \\ \mathbf{F}_I^* &= \sum_{K=1}^{NP} \Psi_I(\mathbf{x}_K) \mathbf{h}(\mathbf{x}_K) A_K + \sum_{L=1}^{NP} \Psi_I(\mathbf{x}_L) \mathbf{b}(\mathbf{x}_L) V_L, \\ \tilde{\mathbf{F}}_I^* &= \sum_{K=1}^{NP} \Psi_I(\mathbf{x}_K) v_s^w(\mathbf{x}_K) A_K + \sum_{L=1}^{NP} \bar{\mathbf{B}}_I^{p,T}(\mathbf{x}_L) \frac{k}{\mu^w} \rho^w \mathbf{g} V_L \end{aligned} \right\} \quad (76)$$

Nevertheless, low energy modes may still be triggered in transient problems and cause instability; hence, the Modified Stabilized Non-conforming Nodal Integration (MSNNI) [34] improves the stability by adding a penalty-type stabilization term in the internal energy. For the u - p semi-Lagrangian RKPM framework, the terms

$$\tilde{\alpha} \sum_{L=1}^{NP} \sum_{c=1}^{Ns_L} \left(\bar{\mathbf{B}}_I^T(\mathbf{x}_L) - \bar{\mathbf{B}}_I^T(\mathbf{x}_c) \right) \mathbf{C} \left(\bar{\mathbf{B}}_J(\mathbf{x}_L) - \bar{\mathbf{B}}_J(\mathbf{x}_c) \right) V_c \mathbf{d}_J^{n+1} \quad (77)$$

$$\text{and} \quad \tilde{\alpha}^p \sum_{L=1}^{NP} \sum_{c=1}^{Ns_L} \left(\bar{\mathbf{B}}_I^{p,T}(\mathbf{x}_L) - \bar{\mathbf{B}}_I^{p,T}(\mathbf{x}_c) \right) \frac{k}{\mu^w} \left(\bar{\mathbf{B}}_J^p(\mathbf{x}_L) - \bar{\mathbf{B}}_J^p(\mathbf{x}_c) \right) V_c p_J^{n+1} \quad (78)$$

are added in $\mathbf{F}_I^{\text{int}}$ and $\tilde{\mathbf{F}}_I^{\text{int}}$, respectively, in Eq. (75), and the terms

$$\tilde{\alpha} \sum_{L=1}^{NP} \sum_{c=1}^{Ns_L} \left(\bar{\mathbf{B}}_I^T(\mathbf{x}_L) - \bar{\mathbf{B}}_I^T(\mathbf{x}_c) \right) \mathbf{C} \left(\bar{\mathbf{B}}_J(\mathbf{x}_L) - \bar{\mathbf{B}}_J(\mathbf{x}_c) \right) V_c \quad (79)$$

$$\text{and} \quad \tilde{\alpha}^p \sum_{L=1}^{NP} \sum_{c=1}^{Ns_L} \left(\bar{\mathbf{B}}_I^{p,T}(\mathbf{x}_L) - \bar{\mathbf{B}}_I^{p,T}(\mathbf{x}_c) \right) \frac{k}{\mu^w} \left(\bar{\mathbf{B}}_J^p(\mathbf{x}_L) - \bar{\mathbf{B}}_J^p(\mathbf{x}_c) \right) V_c \quad (80)$$

are added in \mathbf{K}_{IJ} and H_{IJ} , respectively, in Eq. (76), where $\tilde{\alpha}$ and $\tilde{\alpha}^p$ are the stabilization parameters ranging between 0 and 1, \mathbf{C} is the elastic material tangent tensor, V_c is the nodal volume associated with subdomain c (see Figure 2b), $\sum_{c=1}^{Ns_L} V_c = V_L$, and Ns_L is the number of subdomains in the nodal representative domain of node L .

4.4 Kernel Contact Algorithms for the u - p semi-Lagrangian RKPM

Another advantage of the semi-Lagrangian RK shape function is that it can be used to naturally detect the contacting bodies without the necessity of pre-defined contacting surfaces as in conventional contact algorithms [51]. This trait has considerable benefits for modeling contact problems involving arbitrary new free surface formation, such as penetration and landslide problems. The natural kernel contact algorithm [33] uses the partition of unity of semi-

Lagrangian RK shape functions, i.e. $\sum_{I=1}^{NP} \Psi_I(\mathbf{x}) = 1$, as a contact detection algorithm to determine contact between two bodies (Figure 3). When the partition of unity is formed between contacting surfaces, the contacting bodies are naturally considered as a single continuum body. Hence, the contact forces are directly determined from pair-wise compressive stresses induced by the overlapping of the semi-Lagrangian RK shape functions, which naturally prevents interpenetration between contacting bodies.

In this paper, we only consider contact for the case of dynamic u - p formulation using the explicit temporal integration as it is the only framework to be used for landslide simulations due to its significantly superior computational efficiency over the implicit temporal integration. For the u - p semi-Lagrangian RKPM framework, the contact force acting on point I ($\mathbf{F}_I^{\text{cont}}$) is computed from the pair-wise compressive effective stress, that is

$$\mathbf{F}_I^{\text{cont}} = \sum_{L \in N_I^*} \bar{\mathbf{B}}_I^T(\mathbf{x}_L) \bar{\boldsymbol{\sigma}}(\mathbf{x}_L) V_L \quad ; \quad \mathbf{n}_{IL} \cdot \bar{\boldsymbol{\sigma}}(\mathbf{x}_L) \cdot \mathbf{n}_{IL} < 0 \quad (81)$$

where \mathbf{n}_{IL} is a unit vector from node L to node I , N_I^* is the set of nodal points in the body that does not contain node I . The total force acting on point I ($\mathbf{F}_I^{\text{total}}$) is then computed by the summation of internal force $\mathbf{F}_I^{\text{int}}$ from Eq. (75) and the contact force $\mathbf{F}_I^{\text{cont}}$, that is

$$\mathbf{F}_I^{\text{total}} = \mathbf{F}_I^{\text{int}} + \mathbf{F}_I^{\text{cont}} \quad (82)$$

Although the natural kernel contact algorithm is efficient and naturally enforces the non-penetration condition, the algorithm cannot represent stick and slip conditions as it only considers pair-wise compressive contact forces.

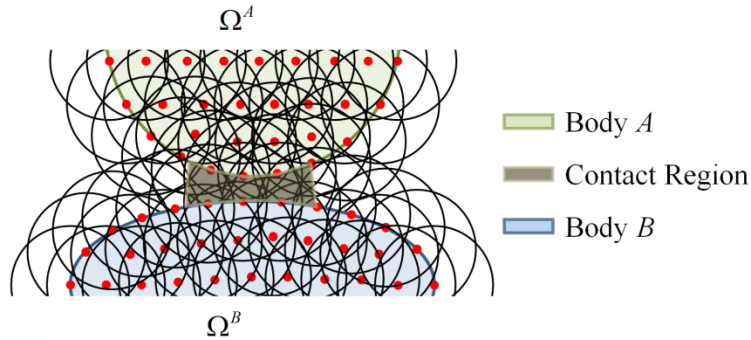


FIG. 3. Contact between two bodies using kernel contact algorithms.

The frictional kernel contact algorithm, which employs the elasto-perfectly-plastic model to represent the friction forces in contact region (Figure 3) by following the Coulomb's law of friction is adopted in this work. The yield surface of the plasticity model is designed such that

elastic region represents stick condition and plastic region represents slip condition. By accounting for friction forces, Eq. (81) is corrected as

$$\mathbf{F}_I^{\text{cont}} = \sum_{L \in N_I^*} \bar{\mathbf{B}}_I^T(\mathbf{x}_L) (\bar{\boldsymbol{\sigma}}(\mathbf{x}_L) + \lambda \boldsymbol{\xi}(\mathbf{x}_L)) V_L \quad ; \quad \mathbf{n}_{IL} \cdot \bar{\boldsymbol{\sigma}}(\mathbf{x}_L) \cdot \mathbf{n}_{IL} < 0 \quad (83)$$

$$\text{with} \quad \lambda = \begin{cases} 0 & ; \text{ elastic} \\ \frac{\mu t_N - \|\mathbf{t}_T\|}{\|\mathbf{t}_T\|} & ; \text{ plastic} \end{cases} \quad (84)$$

$$\text{and} \quad \boldsymbol{\xi}(\mathbf{x}_L) = (\mathbf{n}_{IL} \otimes \bar{\boldsymbol{\sigma}}(\mathbf{x}_L) \cdot \mathbf{n}_{IL} + \mathbf{n}_{IL} \cdot \bar{\boldsymbol{\sigma}}(\mathbf{x}_L) \otimes \mathbf{n}_{IL}) - 2t_N \mathbf{n}_{IL} \otimes \mathbf{n}_{IL} \quad (85)$$

where $t_N = \mathbf{n}_{IL} \cdot \bar{\boldsymbol{\sigma}}(\mathbf{x}_L) \cdot \mathbf{n}_{IL}$ is the amplitude of normal traction, $\mathbf{t}_T = \bar{\boldsymbol{\sigma}}(\mathbf{x}_L) \cdot \mathbf{n}_{IL} - t_N \mathbf{n}_{IL}$ is the tangential traction, and μ is the friction coefficient, which is taken as 0.1 in this paper.

Nevertheless, the pair-wise normal/tangential vector used in the aforementioned kernel contact algorithms is just a simplification, which may not properly represent actual normal/tangential vector of contacting surfaces and can impair the accuracy. The simplified vector is used due to the difficulty of determining physical boundaries in mesh-free discretization. To overcome the issue, a level set algorithm is introduced in [46] to represent contacting surfaces.

The normal contact surface \mathbf{n} can be estimated by the zero level set $\phi(\mathbf{x}) = 0$ as

$$\mathbf{n} = -\frac{\nabla \phi}{\|\nabla \phi\|} \quad \text{on} \quad \phi(\mathbf{x}) = 0 \quad (86)$$

$$\text{with} \quad \phi(\mathbf{x}) = \sum_{I \in N^A \cup N^B} \Psi_I(\mathbf{x}) c_I \quad (87)$$

$$\text{and} \quad c_I = \begin{cases} 1 & ; \quad I \in N^A \\ -1 & ; \quad I \in N^B \end{cases} \quad (88)$$

where N^A and N^B are the sets of nodal points in bodies A and B , respectively. However, it is computationally impractical to explicitly use the zero level set $\phi(\mathbf{x}) = 0$ as a criterion to define normal contact surface; therefore, it is proposed in to search for the zero level set only on the lines that connect a pair of potential contacting nodal points. Ultimately, the contact region or so-called contact processing zone (Figure 3), which is used for calculating friction forces as described above, is defined by the closest layers of nodal points to the contacting surfaces.

5. NUMERICAL EXAMPLES

Six numerical examples are given to verify and validate the performance of the explicit and implicit u - p semi-Lagrangian RKPM frameworks described in Section 4. The first three examples are benchmark problems, in which both explicit and implicit u - p semi-Lagrangian

RKPM frameworks are considered, whereas only explicit framework is considered for the last three examples, which are landslide simulations. Unless otherwise noted, the following setups are used: semi-Lagrangian RKPM with MSNNI, 2^m subdomains per node with stabilization parameters of 0.5, cubic spline function for kernel function, and a normalized support size of 1.5 with linear basis function for semi-Lagrangian RK shape functions.

5.1 Consolidation

A one-dimensional consolidation problem subjected to a step load, $T_0(t) = 1000 \sin(5\pi t)$ when $t < 0.1$ s and $T_0 = 1000$ Pa when $t \geq 0.1$ s, on the top of the column is analyzed. Linear elasticity is employed for the geomaterial response of solid phase and material parameters are given in Table 1. The bottom of the column is fixed and impervious, whereas water can flow out freely ($P=0$) on the top of the column. The column is 30 m in height and is discretized by 61 nodes. The pore water pressure at the point of interest, which is 18 m from the top, is analyzed from 0 to 30 seconds and compared with the analytical solution given in [36]. The accuracy when the row summation method is used for \mathbf{M} and \mathbf{S} (Eqs. (60) and (61)) in the explicit temporal integration is also verified by comparing with the result when using consistent \mathbf{M} and \mathbf{S} .

Problem	5.1	5.2	5.3
Young's Modulus (Pa), E	3×10^7	2.23×10^7	2.5×10^7
Poisson's Ratio, ν	0.2	0.2	0.3
Density (kg/m^3), ρ	1700	1670	2670
Biot Coefficient, α	1	1	1
Biot Compressibility Modulus (Pa), M	3.33×10^8	1×10^{10}	1.1×10^{16}
Permeability $\left(\frac{\text{m}^2}{\text{Pa} \cdot \text{s}} \right), \frac{k}{\mu^w}$	1.02×10^{-6}	1×10^{-6}	1×10^{-7}

Table 1. Material parameters of the one- and two-dimensional problems.

From Figure 4, the results from the explicit and implicit u - p semi-Lagrangian RKPM agree well with the analytical solution. Oscillations occur at the beginning of the consolidation when the explicit temporal integration is used; nonetheless, the oscillations taper off in a few seconds and the results are in good agreement with the analytical solution. It is noted that the oscillations at the beginning of the results are due to the use of explicit temporal integration. Implicit integration, by contrast, shows no numerical oscillation [36]. The detailed study and discussions of the oscillations in this problem and the choice of Newmark parameters to achieve numerical damping, can be found in [36]. Further, while the difference of solutions between the use of the

lumped scheme and the use of consistent matrices with the explicit temporal integration is subtle (Figure 4), the lumped scheme offers significantly better temporal stability over the consistent counterpart, as shown in [46].

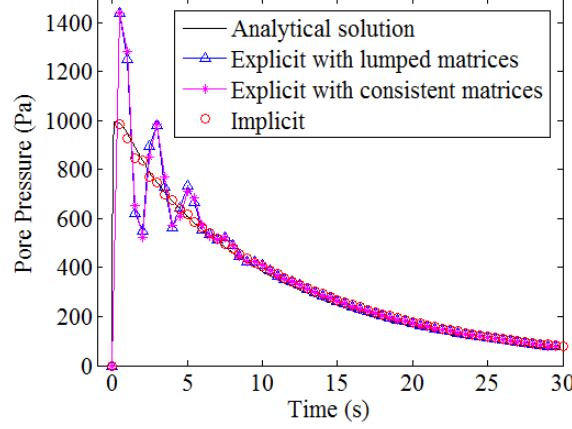


FIG. 4. Semi-Lagrangian RKPM results of the one-dimensional consolidation problem.

5.2 Soil Column with a Sinusoidal Loading

A one-dimensional soil column subjected to a sinusoidal loading, $T_0(t) = 1000(1 - \cos 16\pi t)$ N, on the top of the column is analyzed. Material parameters are given in Table 1, whereas the Biot compressibility modulus M is set to a large value to represent nearly incompressible porous media. Linear elasticity is employed for the geomaterial response of solid phase. The analytical solution of the problem for the fluid-saturated incompressible porous media can be found in [52], which is given as (see Appendix A for more details)

$$u(x, t) = -\frac{1}{\sqrt{a}(\lambda^s + 2\mu^s)} \int_0^t T_0(t - \tau) e^{-\frac{b}{2a}\tau} I_0\left(\frac{b\sqrt{\tau^2 - ax^2}}{2a}\right) U(\tau - \sqrt{a}x) d\tau \quad (89)$$

The above equation is directly employed as the boundary condition for displacement on the bottom of the column, while the top of the column is pervious and the bottom of the column is impervious. The soil column is 10 m in height and is discretized by 21 nodes. Displacement histories of the top node are plotted against the analytical solution from [52]. From Figure 5, the results from the explicit and implicit u - p semi-Lagrangian RKPM agree well with the analytical solution. No numerical oscillation is observed in the results.

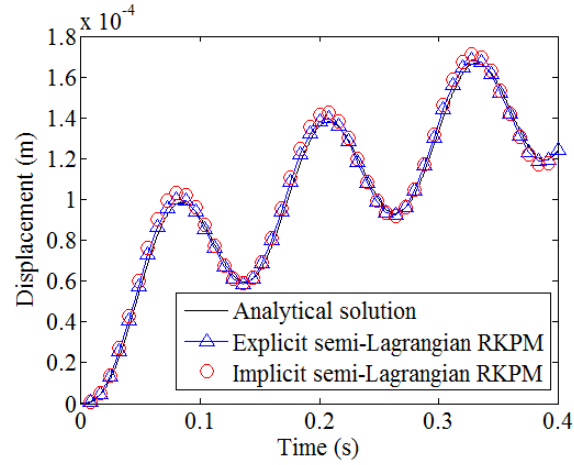


FIG. 5. Displacement histories at the top of the soil column.

5.3 Footing Load on Semi-Infinite Soil

A two-dimensional strip load on infinite half-space as shown in Figure 6, where the boundary conditions for displacement and pore pressure are depicted, is analyzed. Linear elasticity is employed for the geomaterial response of solid phase and material parameters are given in Table 1 [53]. The problem is discretized by 61 nodes on each direction. The stability of the u - p semi-Lagrangian RKPM with MSNNI, when equal-order interpolation is used, is demonstrated in this problem by comparing the contour plot of the pore pressure with conventional FEM result [53].

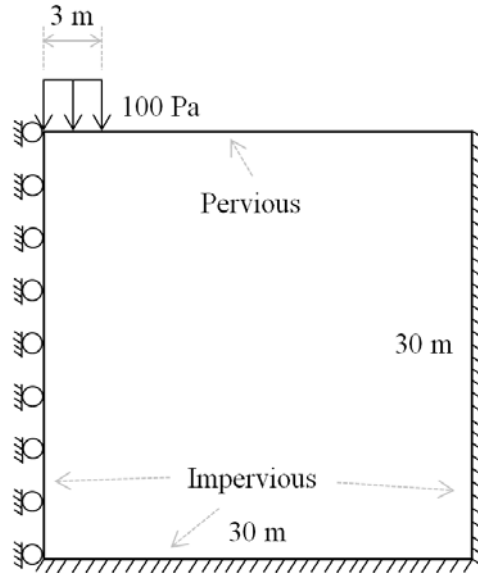


FIG. 6. Schematic of a strip load on infinite half-space.

Figure 7a shows that a stable pore pressure distribution can be obtained by using equal-order u - p semi-Lagrangian RKPM with MSNNI and an implicit temporal integration scheme, whereas an oscillatory result is obtained from Q1-P1 FEM (cf. [53]). However, when the explicit temporal integration is used, temporal instability is observed in the u - p semi-Lagrangian RKPM result. The observation agrees with the von Neumann prediction given in that the unconditionally unstable result is expected for the set of material parameters used in this problem, when explicit temporal integration is employed. Subsequently, when the Biot compressibility modulus M is reduced to 1.1×10^{12} , a stable and smooth result is obtained in Figure 7b.

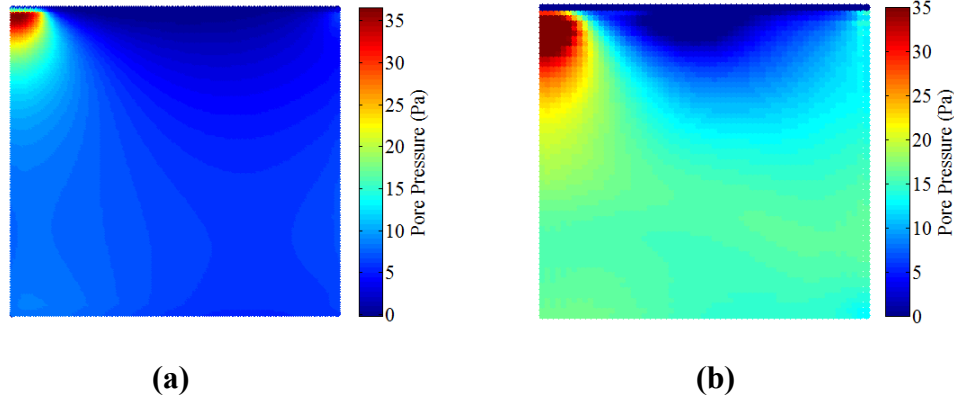


FIG. 7. Contour plots of pore pressure using equal-order semi-Lagrangian RKPM with MSNNI. (a) Using the implicit temporal integration and the set of material parameters in Table 1; (b) Using the explicit temporal integration and a reduced compressibility modulus.

5.4 Slope Stability Analysis

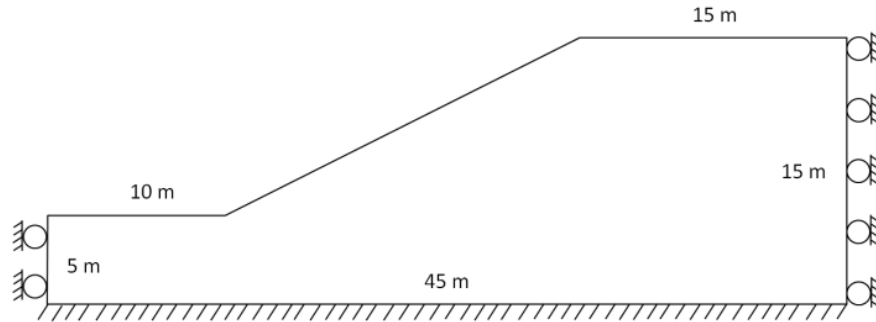


FIG. 8. Schematic of a slope.

The explicit u - p semi-Lagrangian RKPM is employed to analyze stability of a slope (Figure 8) under dry conditions ($p=0$) by verifying the result with FEM [54]. The critical value of cohesion, when slope is unstable as reported in [54], is employed (Table 2) to compare the slip surface. Other parameters used in this study are identical to that in [54], which are for Drucker-Prager

with associated flow rule. The only difference is the use of damage model in the proposed method to determine the slip surface instead of the slip circle analysis used in [54]. The problem is discretized by 25,588 nodes.

Young's Modulus (Pa), E	2×10^8
Poisson's Ratio, ν	0.25
Density (kg/m ³), ρ	2039
Cohesion (Pa), c	2000
Friction Angle ($^\circ$), ϕ	20
Damage Parameter: Initiation, c_2	0.05
Damage Parameter: Critical, c_1	1

Table 2. Material properties of the slope.

The slip surface and displacement contour of the result from FEM [54] are illustrated in Figure 9 by black solid lines and arrows, which are placed on top of the result from semi-Lagrangian RKPM. It can be seen from Figure 9 that the slip surface from semi-Lagrangian RKPM agrees well with the result from FEM, which verifies the capability of the framework to effectively analyzing slope stability.

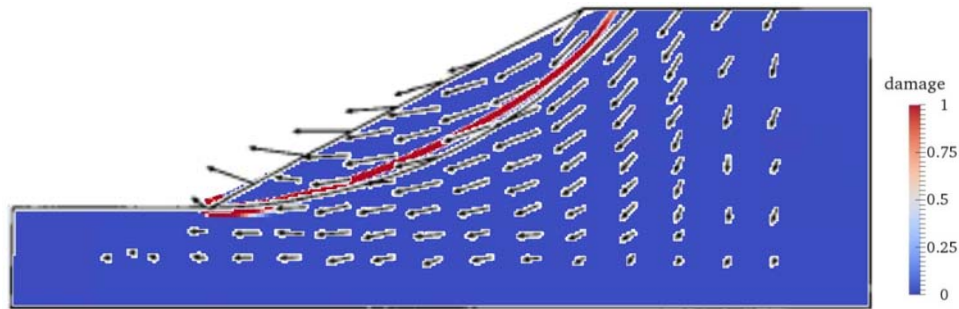


FIG. 9. Comparison between the results from FEM with slip circle analysis (black) and semi-Lagrangian RKPM with damage model (color).

5.5 Vertical-Cut Slope

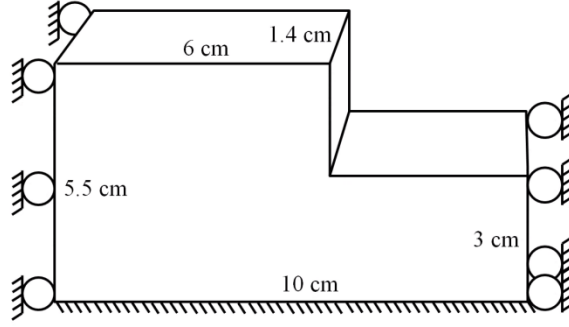


FIG. 10. Schematic of a vertical-cut slope.

A validation of a landslide simulation using the explicit u - p semi-Lagrangian RKPM is conducted by comparing the simulation of a three-dimensional vertical-cut slope (Figure 10) with the experimental result from a centrifuge test [55]. The vertical-cut slope is made of soft clay and is put under the centrifugal acceleration of 150 times of the gravitational acceleration. The behaviors of solid phase of porous media are represented by a Drucker-Prager plasticity with damage model as described in Section 2, and material parameters are given in Table 3. The boundary conditions for displacement are shown in Figure 10. In addition, the bottom, left, and rightmost boundaries are impervious and the other boundaries are pervious. The problem is discretized by 97,776 nodes.

Young's Modulus (Pa), E	4×10^6
Poisson's Ratio, ν	0.2
Density (kg/m^3), ρ	2000
Biot Coefficient, α	1
Biot Compressibility Modulus (Pa), M	3.33×10^7
Permeability $\left(\frac{\text{m}^2}{\text{Pa} \cdot \text{s}} \right)$, $\frac{k}{\mu^w}$	1×10^{-6}
Cohesion (Pa), c	3×10^4
Friction Angle ($^\circ$), ϕ	15
Dilatancy Angle ($^\circ$), ψ	0
Damage Parameter: Initiation, c_2	0.1
Damage Parameter: Critical, c_1	1

Table 3. Material parameters of the vertical-cut slope.

The simulation results from the explicit u - p semi-Lagrangian RKPM (Figure 11) shows similar failure patterns and deposition as in the experimental result from a centrifuge test (Figure 12).

This problem demonstrates that the two-field semi-Lagrangian RKPM can determine accurate slip surface and predict landslide propagation.

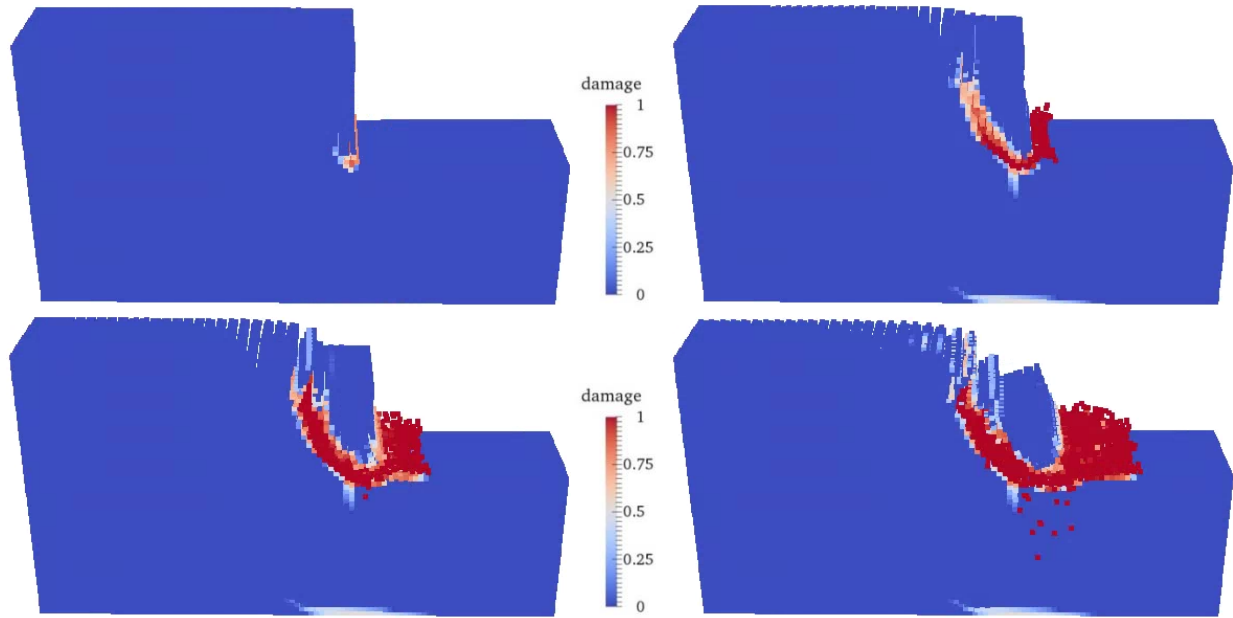


FIG. 11. Progressive deformation and damage of the u - p semi-Lagrangian RKPM landslide simulation of the vertical-cut slope.

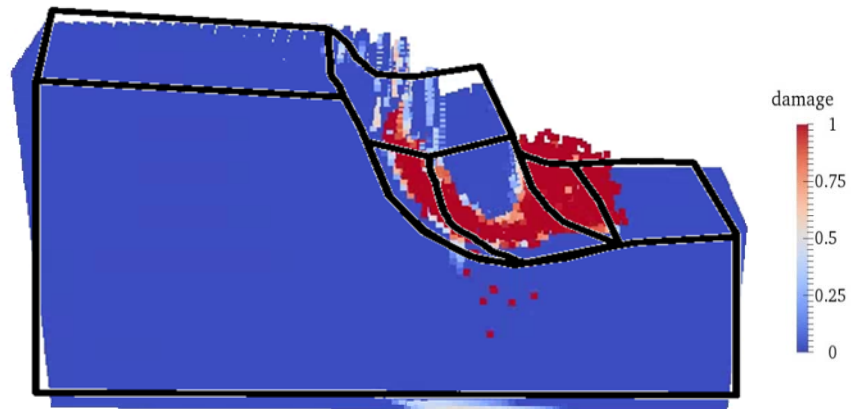


FIG. 12. Comparison of the numerical result from the u - p semi-Lagrangian RKPM to a sketch of the experimental result from [55].

5.6 Landslide at the Reservoir Area of Xiangjiaba, China

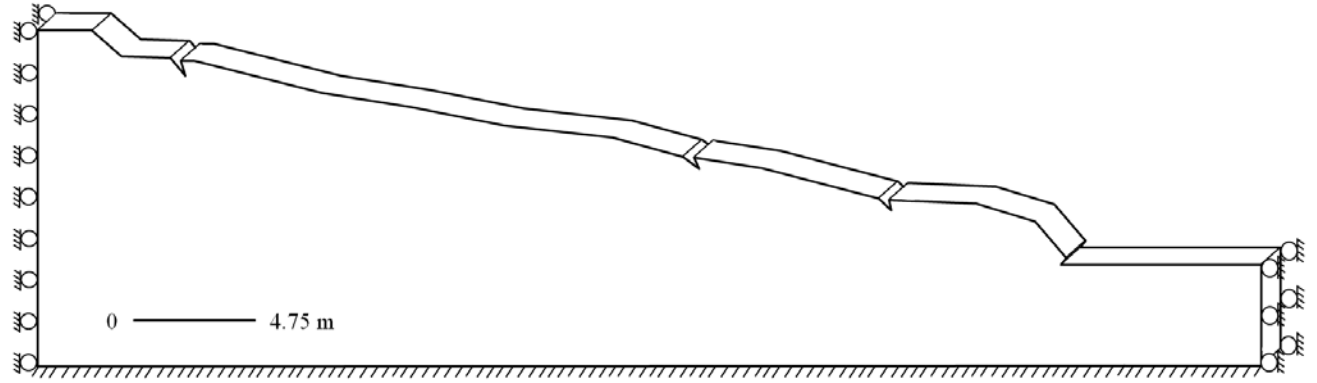


FIG. 13. Problem setup of a three-dimensional landslide simulation.

Young's Modulus (Pa), E	3.5×10^7
Poisson's Ratio, ν	0.35
Density (kg/m^3), ρ	2200
Biot Coefficient, α	1
Biot Compressibility Modulus (Pa), M	3.33×10^6
Permeability $\left(\frac{\text{m}^2}{\text{Pa} \cdot \text{s}} \right)$, $\frac{k}{\mu^w}$	1×10^{-6}
Cohesion (Pa), c	1.02×10^4
Friction Angle ($^\circ$), ϕ	10.6
Dilatancy Angle ($^\circ$), ψ	0
Damage Parameter: Initiation, c_2	0.05
Damage Parameter: Critical, c_1	0.5

Table 4. Material parameters of the three-dimensional landslide simulation.

A three-dimensional landslide simulation with problem setup as shown in Figure 13 and material properties in Table 4 is modeled to validate the result with the landslide occurred at a reservoir area in Xiangjiaba, China. The occurrence of the landslide is due to the excavation at the toe of the slope (Figure 13) under rainfall conditions [56]. The problem setup and material parameters used in the simulation is taken directly from the information given in [56], where the gaps on the top of the slope in Figure 13 are used to represent initial soil cracks, which were observed before the landslide occurred. The behaviors of solid phase of porous media are represented by the Drucker-Prager plasticity with damage model. The top boundary is pervious, whereas other boundaries are impervious. The problem is discretized by 99,426 nodes.

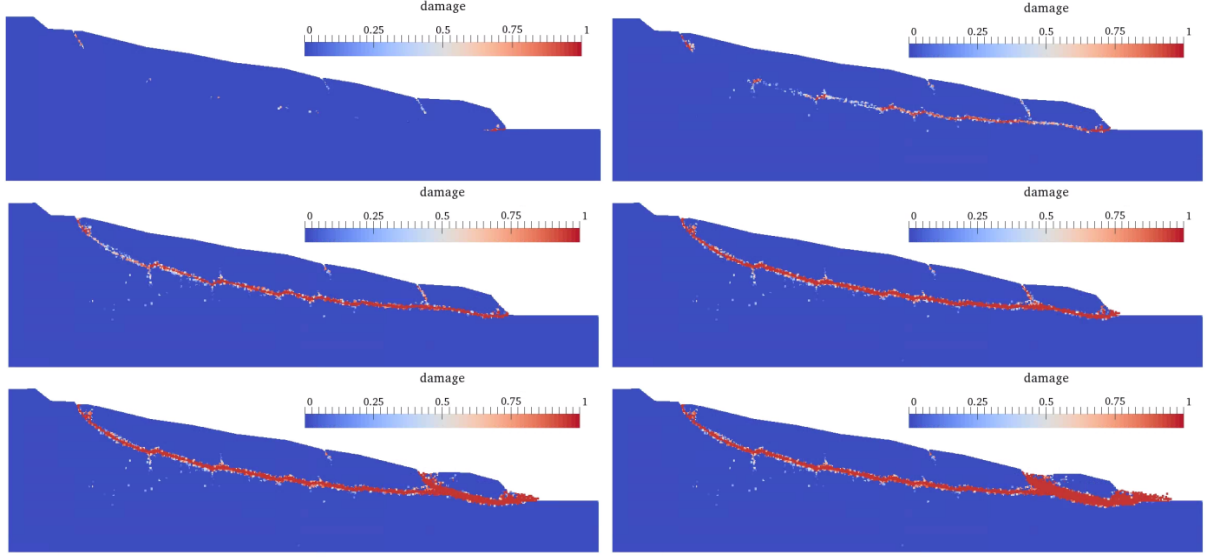


FIG. 14. u - p semi-Lagrangian RKPM landslide simulation of the landslide in Xiangjiaba.

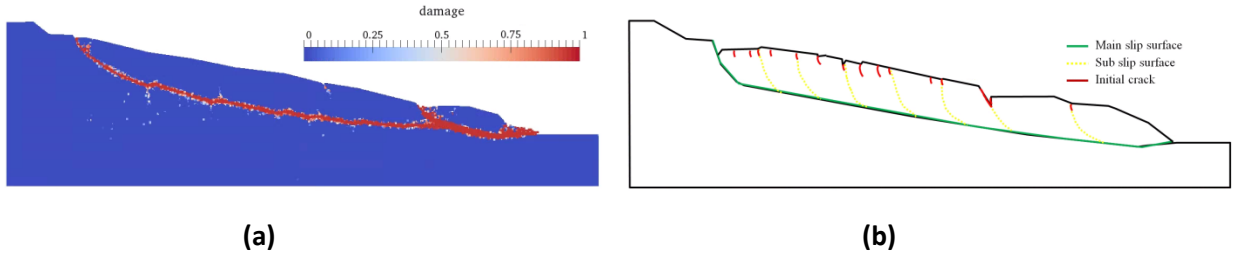


FIG. 15. Comparison between (a) simulation from the u - p semi-Lagrangian RKPM and (b) sketch of the landslide at a reservoir area in Xiangjiaba, China.

The results from the explicit u - p semi-Lagrangian RKPM (Figure 14) demonstrate the capability of the framework for the simulation of full-scale landslide processes. The main slip surface from the simulation (Figure 14) and deposition at the toe also matches well with the sketch of the actual landslide from [56] (Figure 15). It is noted, nevertheless, that the simulation cannot capture the sub-slip surfaces since homogeneous material properties are assumed in the numerical analysis, whereas the soil slope in the actual site has heterogeneous or localized soil mechanical properties.

6. CONCLUSIONS

This paper presents a u - p semi-Lagrangian RK formulation to effectively model landslide processes from the pre-failure to post-failure. The dynamic Biot equation for saturated porous

media is formulated under the semi-Lagrangian RK formulation, where material response of solid phase of porous media is described by a Drucker-Prager plasticity with damage model to properly represent geomaterial behaviors from small deformation to failure. Under the present framework, severe deformation, material separation, and contacts between fragmented bodies, can be handled with relative ease by taking the advantage of the nature of semi-Lagrangian RK shape functions that are constructed based on sets of material points in the current configuration. In addition, the frictional kernel contact algorithm is implemented in the u - p formulation to properly represent interaction between fragmentations and debris in order to capture the post-failure mechanics of landslide events. The Modified Stabilized Non-Conforming Nodal Integration (MSNNI) is also extended to the u - p semi-Lagrangian RK formulation to suppress the spurious low energy modes due to under-integration of the direct nodal integration method. It is noteworthy that when an equal-order interpolation is used for displacement and pore pressure, no significant pressure oscillation has been observed in the numerical study. The explicit temporal integration is employed in the framework for efficiency, and the effect of using row summation for matrices \mathbf{M} and \mathbf{S} on accuracy is shown to be trivial. The temporal stability of the present framework has been analyzed and presented in a separate work. In contrast, the implicit temporal integration offers better temporal stability; however, it is suitable for quasi-static problems or small-scale problems since the computational cost is considerably higher than the explicit time integration for dynamic simulations. The results obtained from the present method are verified with analytical solutions and FEM results. Further, landslide simulations from the present method are validated against the experimental result and field data. The slip surfaces as well as landslide depositions from the simulations qualitatively agree with the experimental result and field data.

Acknowledgement

This research was partially supported by U.S. Army Corps of Engineers (Grant No. W912HQ-16-P-0002).

APPENDIX A

An analytical solution for the displacement of a fluid-saturated incompressible porous media subjected to a loading function $T_0(t)$ on top is given as

$$u(x, t) = -\frac{1}{\sqrt{a}(\lambda^s + 2\mu^s)} \int_0^t T_0(t - \tau) e^{-\frac{b}{2a}\tau} I_0\left(\frac{b\sqrt{\tau^2 - ax^2}}{2a}\right) U(\tau - \sqrt{a}x) d\tau \quad (90)$$

with

$$a = \frac{(n^S)^2 \rho^F + (n^F)^2 \rho^S}{(n^F)^2 (\lambda^S + 2\mu^S)} \quad (91)$$

$$b = \frac{S_v}{(n^F)^2 (\lambda^S + 2\mu^S)} \quad (92)$$

$$S_v = \frac{(n^F)^2 \gamma^{FR}}{k^F} \quad (93)$$

where I_0 is the modified Bessel function of the first kind of zero order and $U(t)$ is the Heaviside function. The parameters used in above equations are taken from [52]. The relationships of the parameters used herein and those used in can be found in Table A.1, which has been used for the second numerical example to convert material parameters from [52] (Table A.2) into material parameters used in this paper (Table 1).

Parameters in [52]	Parameters in this paper
n^S	$1-n$
n^F	n
$\rho^S + \rho^F$	ρ
E	$E/(1-n)$
ν	ν
k^F	$(k/\mu^w) \rho^w g$
γ^{FR}	$\rho^w g$

Table A.1 Relationships of parameters.

$n^S = 0.67$	$n^F = 0.33$
$\rho^S = 1.34 \times 10^3 \text{ kg/m}^3$	$\rho^F = 0.33 \times 10^3 \text{ kg/m}^3$
$E = 3 \times 10^7 \text{ Pa}$	$\nu = 0.2$
$\lambda^S = 5.5833 \times 10^6 \text{ Pa}$	$\mu^S = 8.375 \times 10^6 \text{ Pa}$
$k^F = 1 \times 10^{-2} \text{ m/s}$	$\gamma^{FR} = 1 \times 10^4 \text{ N/m}^3$

Table A.2 Parameters used in [52].

APPENDIX B

To show the effect of convective terms arising from semi-Lagrangian kernels on the solution (Eqs. (46)-(47)), the following one-dimensional wave equation is considered:

$$\rho \ddot{u} - E u_{,xx} = 0, \quad x \in (0, L), \quad t \in [0, T) \quad (94)$$

with boundary and initial conditions,

$$\begin{aligned} u_{,x}(0, t) &= k \sin(\omega t) \\ u_{,x}(L, t) &= k \cos(kL) \sin(\omega t) \\ u(x, 0) &= 0 \\ \dot{u}(x, 0) &= \omega \sin(kx) \end{aligned} \quad (95)$$

The analytical solution for this problem is $u(x, t) = \sin(\omega t) \sin(kx)$, where $\omega = m\pi c/L$,

$k = \omega/c$, $c = \sqrt{E/\rho}$, and m is a positive integer. Here $m=5$, $L=40$, $E=1$, and $\rho=10$ are chosen.

The domain is uniformly discretized with 41 nodes. The linear RK with 1.5 normalized support is used as the shape function and the SCNI is employed for the domain integration, following the procedures given in Section 3. The central difference scheme with a time step of 0.1 is employed for temporal integration. Three numerical solutions obtained from different formulations are at $t=4$ given in Fig. 16 for comparison: 1) total Lagrangian, 2) semi-Lagrangian RK, and 3) semi-Lagrangian RK without convective terms. As can be seen in Fig. 16, the semi-Lagrangian RK solutions are in agreement with the analytical solution, and the difference between the semi-Lagrangian RK with and without convective are relatively small.

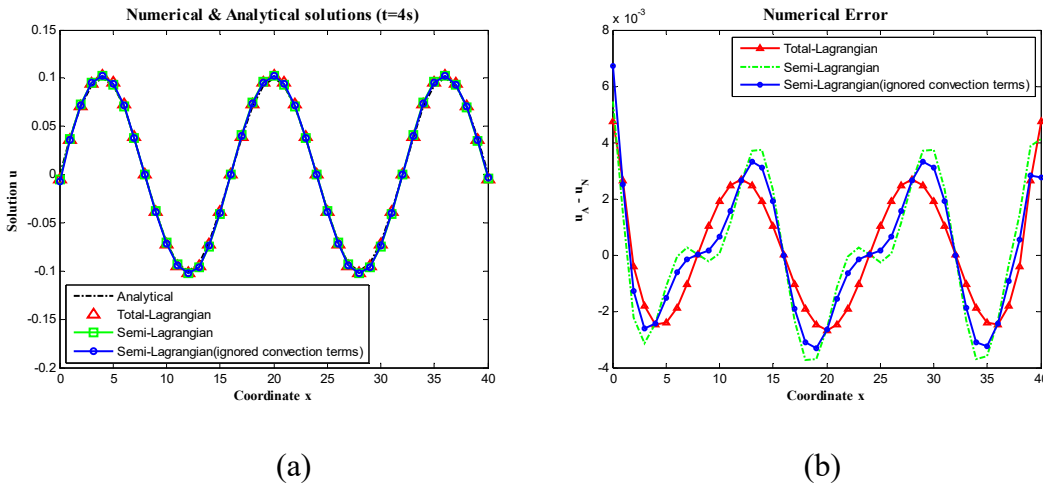


FIG. 16. Semi-Lagrangian RK solutions for one-dimensional wave propagation.

REFERENCES

1. Borja, R.I. and J.A. White, *Continuum deformation and stability analyses of a steep hillside slope under rainfall infiltration*. Acta Geotechnica, 2010. **5**(1): p. 1-14.
2. Feng, X. and A. Guo. *Earthquake landslides in China*. in the *4th International Conference and Field Workshop on Landslides*. 1985.
3. Borja, R.I., X.Y. Liu, and J.A. White, *Multiphysics hillslope processes triggering landslides*. Acta Geotechnica, 2012. **7**(4): p. 261-269.
4. Petley, D., *Global patterns of loss of life from landslides*. Geology, 2012. **40**(10): p. 927-930.
5. Huang, Y.H., *Slope Stability Analysis by the Limit Equilibrium Method: Fundamentals and Methods*. 2014, ASCE Press.
6. Cho, S.E. and S.R. Lee, *Instability of unsaturated soil slopes due to infiltration*. Computers and Geotechnics, 2001. **28**(3): p. 185-208.
7. Conte, E., A. Donato, and A. Troncone, *A finite element approach for the analysis of active slow-moving landslides*. Landslides, 2014. **11**(4): p. 723-731.
8. Pastor, M., B. Haddad, G. Sorbino, S. Cuomo, and V. Drempetic, *A depth-integrated, coupled SPH model for flow-like landslides and related phenomena*. International Journal for Numerical and Analytical Methods in Geomechanics, 2009. **33**(2): p. 143-172.
9. Huang, Y., W.J. Zhang, Q. Xu, P. Xie, and L. Hao, *Run-out analysis of flow-like landslides triggered by the Ms 8.0 2008 Wenchuan earthquake using smoothed particle hydrodynamics*. Landslides, 2012. **9**(2): p. 275-283.
10. Hungr, O. and S. McDougall, *Two numerical models for landslide dynamic analysis*. Computers & Geosciences, 2009. **35**(5): p. 978-992.
11. Rodriguez-Paz, M.X. and J. Bonet, *A corrected smooth particle hydrodynamics method for the simulation of debris flows*. Numerical Methods for Partial Differential Equations, 2004. **20**(1): p. 140-163.
12. McDougall, S. and O. Hungr, *A model for the analysis of rapid landslide motion across three-dimensional terrain*. Canadian Geotechnical Journal, 2004. **41**(6): p. 1084-1097.
13. Bui, H.H., R. Fukagawa, K. Sako, and S. Ohno, *Lagrangian meshfree particles method (SPH) for large deformation and failure flows of geomaterial using elastic-plastic soil constitutive model*. International Journal for Numerical and Analytical Methods in Geomechanics, 2008. **32**(12): p. 1537-1570.
14. Ataie-Ashtiani, B. and G. Shobeyri, *Numerical simulation of landslide impulsive waves by incompressible smoothed particle hydrodynamics*. International Journal for Numerical Methods in Fluids, 2008. **56**(2): p. 209-232.
15. Campbell, C.S., P.W. Cleary, and M. Hopkins, *Large-Scale Landslide Simulations - Global Deformation, Velocities and Basal Friction*. Journal of Geophysical Research-Solid Earth, 1995. **100**(B5): p. 8267-8283.
16. Tang, C.L., J.C. Hu, M.L. Lin, J. Angelier, C.Y. Lu, Y.C. Chan, and H.T. Chu, *The Tsaoling landslide triggered by the Chi-Chi earthquake, Taiwan: Insights from a discrete element simulation*. Engineering Geology, 2009. **106**(1-2): p. 1-19.
17. Cleary, P.W. and C.S. Campbell, *Self-Lubrication for Long Runout Landslides - Examination by Computer-Simulation*. Journal of Geophysical Research-Solid Earth, 1993. **98**(B12): p. 21911-21924.
18. Gingold, R.A. and J.J. Monaghan, *Smoothed Particle Hydrodynamics - Theory and Application to Non-Spherical Stars*. Monthly Notices of the Royal Astronomical Society, 1977. **181**(2): p. 375-389.

19. Cundall, P.A. and O.D.L. Strack, *A Discrete Numerical-Model for Granular Assemblies - Reply*. Geotechnique, 1980. **30**(3): p. 335-336.
20. Yan, Z., S.K. Wilkinson, E.H. Stitt, and M. Marigo, *Discrete element modelling (DEM) input parameters: understanding their impact on model predictions using statistical analysis*. Computational Particle Mechanics, 2015. **2**(3): p. 283–299.
21. Pastor, M., D. Manzanal, J.A.F. Merodo, P. Mira, T. Blanc, V. Drempetic, M.J. Pastor, B. Haddad, and M. Sanchez, *From solids to fluidized soils: diffuse failure mechanisms in geostructures with applications to fast catastrophic landslides*. Granular Matter, 2010. **12**(3): p. 211-228.
22. Eberhardt, E., D. Stead, and J.S. Coggan, *Numerical analysis of initiation and progressive failure in natural rock slopes - the 1991 Randa rockslide*. International Journal of Rock Mechanics and Mining Sciences, 2004. **41**(1): p. 69-87.
23. Stead, D., E. Eberhardt, and J.S. Coggan, *Developments in the characterization of complex rock slope deformation and failure using numerical modelling techniques*. Engineering Geology, 2006. **83**(1-3): p. 217-235.
24. Cuomo, S., N. Prime, A. Iannone, F. Dufour, L. Cascini, and F. Darve, *Large deformation FEM-LIP drained analysis of a vertical cut*. Acta Geotechnica, 2013. **8**(2): p. 125-136.
25. Prime, N., F. Dufour, and F. Darve, *Solid-fluid transition modelling in geomaterials and application to a mudflow interacting with an obstacle*. International Journal for Numerical and Analytical Methods in Geomechanics, 2014. **38**(13): p. 1341-1361.
26. Liu, W.K., S. Jun, and Y.F. Zhang, *Reproducing Kernel Particle Methods*. International Journal for Numerical Methods in Fluids, 1995. **20**(8-9): p. 1081-1106.
27. Chen, J.S., C.H. Pan, C.T. Wu, and W.K. Liu, *Reproducing kernel particle methods for large deformation analysis of non-linear structures*. Computer Methods in Applied Mechanics and Engineering, 1996. **139**(1-4): p. 195-227.
28. Melenk, J.M. and I. Babuska, *The partition of unity finite element method: Basic theory and applications*. Computer Methods in Applied Mechanics and Engineering, 1996. **139**(1-4): p. 289-314.
29. Chen, J.S., C. Pan, and C.T. Wu, *Large deformation analysis of rubber based on a reproducing kernel particle method*. Computational Mechanics, 1997. **19**(3): p. 211-227.
30. Wang, D.D., Z.Y. Li, L. Li, and Y.C. Wu, *Three dimensional efficient meshfree simulation of large deformation failure evolution in soil medium*. Science China-Technological Sciences, 2011. **54**(3): p. 573-580.
31. Chi, S.W., C.H. Lee, J.S. Chen, and P.C. Guan, *A level set enhanced natural kernel contact algorithm for impact and penetration modeling*. International Journal for Numerical Methods in Engineering, 2015. **102**(3-4): p. 839-866.
32. Guan, P.C., J.S. Chen, Y. Wu, H. Teng, J. Gaidos, K. Hofstetter, and M. Alsaleh, *Semi-Lagrangian reproducing kernel formulation and application to modeling earth moving operations*. Mechanics of Materials, 2009. **41**(6): p. 670-683.
33. Guan, P.C., S.W. Chi, J.S. Chen, T.R. Slawson, and M.J. Roth, *Semi-Lagrangian reproducing kernel particle method for fragment-impact problems*. International Journal of Impact Engineering, 2011. **38**(12): p. 1033-1047.
34. Chen, J.S., W. Hu, M.A. Puso, Y. Wu, and X. Zhang, *Strain smoothing for stabilization and regularization of Galerkin meshfree methods*, in *Meshfree Methods for Partial Differential Equations III*. 2007, Springer. p. 57–75.

35. Zienkiewicz, O.C., A.H.C. Chan, M. Pastor, B.A. Schrefler, and T. Shiomi, *Computational geomechanics*. 1999, Chichester: Wiley.
36. Zienkiewicz, O.C. and T. Shiomi, *Dynamic Behavior of Saturated Porous-Media - the Generalized Biot Formulation and Its Numerical-Solution*. International Journal for Numerical and Analytical Methods in Geomechanics, 1984. **8**(1): p. 71-96.
37. Ju, J.W., *On Energy-Based Coupled Elastoplastic Damage Theories - Constitutive Modeling and Computational Aspects*. International Journal of Solids and Structures, 1989. **25**(7): p. 803-833.
38. Hughes, T.J.R. and J. Winget, *Finite Rotation Effects in Numerical-Integration of Rate Constitutive-Equations Arising in Large-Deformation Analysis*. International Journal for Numerical Methods in Engineering, 1980. **15**(12): p. 1862-1867.
39. Ladyzhenskaya, O.A., *The mathematical theory of viscous incompressible flow*. Vol. 76. 1969, New York: Gordon and Breach.
40. Babuška, I., *The finite element method with Lagrangian multipliers*. Numerische Mathematik, 1973. **20**(3): p. 179-192.
41. Brezzi, F., *On the existence, uniqueness and approximation of saddle-point problems arising from Lagrangian multipliers*. Analyse numérique, 1974. **8**(2): p. 129-151.
42. Wei, H., J.S. Chen, and M. Hillman, *A stabilized nodally integrated meshfree formulation for fully coupled hydro-mechanical analysis of fluid-saturated porous media*. Computers & Fluids, 2016. **141**: p. 105–115.
43. Sun, W.C., J.T. Ostien, and A.G. Salinger, *A stabilized assumed deformation gradient finite element formulation for strongly coupled poromechanical simulations at finite strain*. International Journal for Numerical and Analytical Methods in Geomechanics, 2013. **37**(16): p. 2755-2788.
44. White, J.A. and R.I. Borja, *Stabilized low-order finite elements for coupled solid-deformation/fluid-diffusion and their application to fault zone transients*. Computer Methods in Applied Mechanics and Engineering, 2008. **197**(49-50): p. 4353-4366.
45. Chen, J.S., W.M. Han, Y. You, and X.P. Meng, *A reproducing kernel method with nodal interpolation property*. International Journal for Numerical Methods in Engineering, 2003. **56**(7): p. 935-960.
46. Chi, S.W., T. Sirtakorn, and S.P. Lin, *Von Neumann stability analysis of the u-p reproducing kernel formulation for saturated porous media*. Computational Mechanics, 2016.
47. Hillman, M., J.S. Chen, and S.W. Chi, *Stabilized and variationally consistent nodal integration for meshfree modeling of impact problems*. Computational Particle Mechanics, 2014. **1**(3): p. 245-256.
48. Bonet, J. and S. Kulasegaram, *Correction and stabilization of smooth particle hydrodynamics methods with applications in metal forming simulations*. International Journal for Numerical Methods in Engineering, 2000. **47**(6): p. 1189-1214.
49. Beissel, S. and T. Belytschko, *Nodal integration of the element-free Galerkin method*. Computer Methods in Applied Mechanics and Engineering, 1996. **139**(1-4): p. 49-74.
50. Chen, J.S., C.T. Wu, S. Yoon, and Y. You, *A stabilized conforming nodal integration for Galerkin mesh-free methods*. International Journal for Numerical Methods in Engineering, 2001. **50**(2): p. 435-466.
51. Laursen, T.A., *Computational contact and impact mechanics: fundamentals of modeling interfacial phenomena in nonlinear finite element analysis*. 2013: Springer.

52. Deboer, R., W. Ehlers, and Z.F. Liu, *One-Dimensional Transient Wave-Propagation in Fluid-Saturated Incompressible Porous-Media*. Archive of Applied Mechanics, 1993. **63**(1): p. 59-72.
53. McGann, C.R., P. Arduino, and P. Mackenzie-Helnwein, *Stabilized single-point 4-node quadrilateral element for dynamic analysis of fluid saturated porous media*. Acta Geotechnica, 2012. **7**(4): p. 297-311.
54. Zienkiewicz, O.C., C. Humpheson, and R.W. Lewis, *Associated and Non-Associated Visco-Plasticity and Plasticity in Soil Mechanics*. Geotechnique, 1975. **25**(4): p. 671-689.
55. Allersma, H.G.B., *Small Scale Modelling of Large Granular Systems in a Centrifuge*, in *Traffic and Granular Flow '03*. 2005, Springer. p. 445–458.
56. Xu, L., F.C. Dai, J. Chen, J. Iqbal, and Y.X. Qu, *Analysis of a progressive slope failure in the Xiangjiaba reservoir area, Southwest China*. Landslides, 2014. **11**(1): p. 55-66.